HHS Public Access

Author manuscript

Cell Rep. Author manuscript; available in PMC 2025 May 21.

Published in final edited form as:

Cell Rep. 2025 April 22; 44(4): 115556. doi:10.1016/j.celrep.2025.115556.

The dorsal column nuclei scale mechanical sensitivity in naive and neuropathic pain states

Aman Upadhyay[1,2,3,4,12], **Mark A. Gradwell**[1,2,3,11,12], **Thomas J. Vajtay**[1,2], **James Conner**[5], **Arnab A. Sanyal**[1,2], **Chloe Azadegan**[1,2], **Komal R. Patel**[1,2], **Joshua K. Thackray**[6], **Manon Bohic**[1,2,3], **Fumiyasu Imai**[7,8], **Simon O. Ogundare**[9], **Yutaka Yoshida**[7,8], **Ishmail Abdus-Saboor**[9,10], **Eiman Azim**[5], **Victoria E. Abraira**[1,2,3,11,13,*]

[1]W.M. Keck Center for Collaborative Neuroscience, Rutgers University, The State University of New Jersey, New Brunswick, NJ, USA

[2]Department of Cell Biology and Neuroscience, Rutgers University, The State University of New Jersey, New Brunswick, NJ, USA

[3]Brain Health Institute, Rutgers University, Piscataway, NJ, USA

[4]Graduate Program in Neuroscience, Rutgers Robert Wood Johnson Medical School, Rutgers University, The State University of New Jersey, Piscataway, NJ, USA

[5]Molecular Neurobiology Laboratory, Salk Institute for Biological Studies, La Jolla, CA, USA

[6]Human Genetics Institute of New Jersey, Rutgers University, The State University of New Jersey, Piscataway, NJ, USA

[7]Burke Neurological Institute, White Plains, NY, USA

[8]Brain and Mind Research Institute, Weill Cornell Medicine, New York, NY, USA

[9]Zuckerman Mind Brain Behavior Institute, Columbia University, New York, NY, USA

[10]Department of Biological Sciences, Columbia University, New York, NY, USA

[11]Senior authors

[12]These authors contributed equally

[13]Lead contact

*Correspondence: victoria.abraira@rutgers.edu.

AUTHOR CONTRIBUTIONS

A.U., M.A.G., and V.E.A. conceptualized the study. A.U. performed and analyzed the histology, viral tracing, and behavioral experiments. M.A.G. performed and analyzed the electrophysiology experiments and aided with histology and behavior. J.C. performed and analyzed the *in vivo* recordings. K.R.P. and C.A. aided with the histology and behavior. F.I. performed the cortical viral injections. A.A.S., J.K.T., T.J.V., and S.O.O. assisted with DeepLabCut tracking and PAWS analysis. J.K.T. and A.A.S. performed the B-SOiD analysis. M.B. assisted with the pilot SNI surgeries. E.A., I.A.-S., and Y.Y. provided guidance on the experimental design and interpretation of results. V.E.A. supervised the study. A.U. and M.A.G. wrote the paper, with editing from V.E.A.

DECLARATION OF INTERESTS

The authors declare no competing interests.

SUPPLEMENTAL INFORMATION

Supplemental information can be found online at https://doi.org/10.1016/j.celrep.2025.115556.

SUMMARY

During pathological conditions, tactile stimuli can aberrantly engage nociceptive pathways leading to the perception of touch as pain, known as mechanical allodynia. The brain stem dorsal column nuclei integrate tactile inputs, yet their role in mediating tactile sensitivity and allodynia remains understudied. We found that gracile nucleus (Gr) inhibitory interneurons and thalamus-projecting neurons are differentially innervated by primary afferents and spinal inputs. Functional manipulations of these distinct Gr neuronal populations bidirectionally shifted tactile sensitivity but did not affect noxious mechanical or thermal sensitivity. During neuropathic pain, Gr neurons exhibited increased sensory-evoked activity and asynchronous excitatory drive from primary afferents. Silencing Gr projection neurons or activating Gr inhibitory neurons in neuropathic mice reduced tactile hypersensitivity, and enhancing inhibition ameliorated paw-withdrawal signatures of neuropathic pain and induced conditioned place preference. These results suggest that Gr activity contributes to tactile sensitivity and affective, pain-associated phenotypes of mechanical allodynia.

Graphical abstract

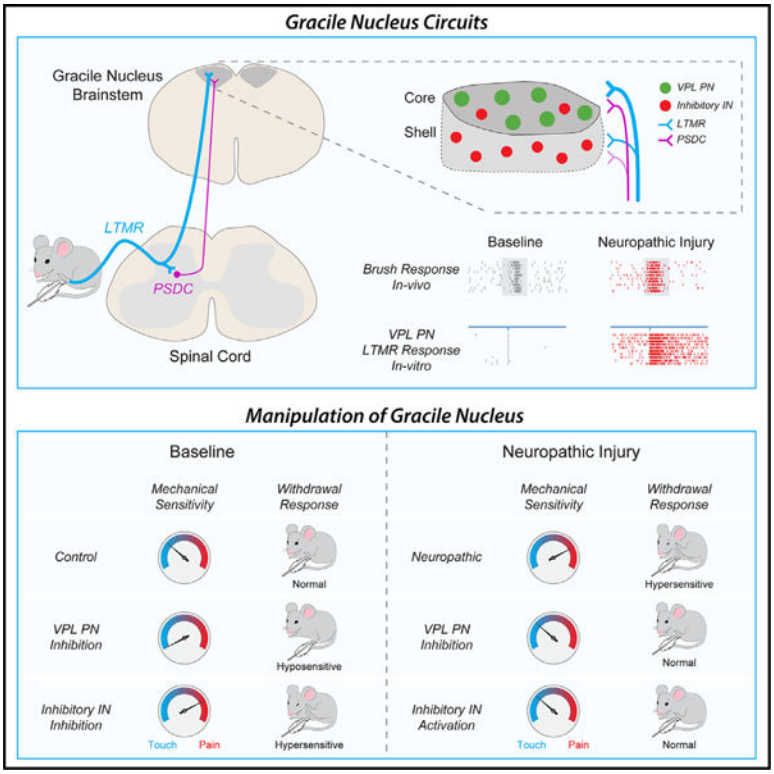

In brief

The role of tactile pathways in allodynia remains understudied. Upadhyay et al. show that the gracile nucleus (Gr) bidirectionally scales tactile sensitivity and becomes hyperexcitable after neuropathic injury. Reducing Gr output alleviates tactile hypersensitivity and affective pain behaviors, highlighting its role in touch-evoked pain (allodynia).

INTRODUCTION

Mechanical allodynia is defined by tactile hypersensitivity and painful responses to innocuous stimuli,[1,2] but we lack a complete understanding of underlying mechanisms and circuits. Studies suggest that allodynia arises from nociceptor sensitization to low-threshold stimuli[3–5] or disruption of spinal circuits that normally gate touch.[6,7] Additionally, the parabrachial nucleus[8,9] and somatosensory cortex[10] have been implicated, suggesting that pathological conditions dysregulate tactile processing across multiple tactile and nociceptive sites. Importantly, transections or nerve blocks of the dorsal root ganglia (DRG) and spinal cord can abolish tactile allodynia,[11–15] underscoring the importance of early sensory pathways. Two early transmitters of tactile information, the DRG and spinal cord, project to the brain stem dorsal column nuclei complex (DCN), which then integrates tactile information and projects to the thalamus.[16,17] However, the circuit organization and functional role of the DCN remain understudied. Notably, DCN blockade in rodents[18] and dorsal column stimulation in humans[19] alleviate neuropathic pain, highlighting the DCN as a clinically relevant but mechanistically understudied target.

DCN neurons exhibit increased spontaneous activity and afterdischarge during inflammatory[20] and neuropathic pain,[21,22] along with increased recruitment following nerve injury.[23,24] Additionally, microglial recruitment[25] and upregulation of neuropeptides[26,27] observed in the nerve-injured spinal cord are mirrored in the DCN.[28,29] Two main pathways innervating the DCN are low-threshold mechanoreceptors (LTMRs) and spinal postsynaptic dorsal column projection neurons (PSDCs). Multiple LTMR subtypes are implicated in mediating allodynia during neuropathic pain,[30–33] and PSDCs, which integrate tactile LTMR inputs, contribute to dorsal column stimulation-induced analgesia.[19] Understanding how these pathways engage DCN circuits in both naive and neuropathic conditions will better inform mechanisms of tactile sensation and allodynia.

DCN processing extends beyond a simple labeled-line transmission model. In macaques, DCN neurons exhibit multimodal responses and complex receptive fields.[34–36] In mice, individual DCN neurons integrate LTMR and PSDC input, with distinct tuning for fine vibrotactile or high-force mechanical stimuli, respectively.[37] Additionally, cortical projections modulate sensory “gain” through local inhibition to generate central-surround receptive fields[38–42] or facilitate sensory feedback-mediated dexterous movement.[43] In the spinal cord, loss of inhibition is a driver of central sensitization during mechanical allodynia,[44–47] enabling tactile input to recruit nociceptive pathways.[6,48–50]

In this study, we investigated how DCN circuits shape tactile sensitivity in naive mice and mechanical allodynia during neuropathic pain. Focusing on the gracile nucleus (Gr), which processes hindlimb tactile information, we found that ventral posterolateral thalamus-projecting neurons (VPL-PNs) and local inhibitory neurons receive distinct inputs from tactile LTMRs and PSDCs. Silencing VPL-PNs reduced tactile sensitivity, while silencing inhibitory neurons induced tactile hypersensitivity and neuropathic pain-like paw-withdrawal signatures. Neuropathic injury increased tactile-evoked Gr activity and excitatory drive onto VPL-PNs. Finally, activating Gr inhibition during neuropathic pain alleviated tactile hypersensitivity and pain-related paw-withdrawal signatures. These

findings demonstrate that the Gr modulates tactile signals in a modality- and intensity-specific manner, contributing to mechanical allodynia during neuropathic pain.

RESULTS

Ascending tactile pathways and descending cortical projections converge in the Gr

In the spinal cord, modality-specific outputs[37,51–55] are dynamically modulated by interneurons,[44,48,56–60] altering tactile transmission[52,61,62] and, in some cases, allowing touch to elicit pain[6,63] or itch.[64–66] However, similar characterizations of the DCN are nascent. The DCN, a key relay in the medial lemniscal pathway, projects to the VPL (Figure 1A). The DCN comprises subnuclei: the Gr receives inputs from below spinal segment T6, while the cuneate nucleus (Cu) receives inputs from above T6.[17] Given the extensive validation of rodent sensory assays and pain models in the hindlimb,[67] our study focused on the Gr.

It is well established that tactile LTMRs and spinal projections, notably PSDCs, target the DCN.[17,37,68] To characterize primary afferent input to the Gr, we injected cholera toxin β subunit (CTb) into the hindpaw, revealing projections within the ipsilateral Gr "core" (Figure 1B). In contrast, genetically labeled primary afferents targeted both the Gr core and a surrounding "shell" region (Figure 1C), suggesting non-hindpaw inputs to the shell. Consistent with the previous literature,[68–70] we observed dense projections from Aβ rapidly adapting-LTMRs (Figure S1A) and Aβ Field-LTMRs (Figure S1B), with limited projections from Aβ slowly adapting-LTMRs (Figure S1C), Aδ-LTMRs (Figure S1D), and proprioceptors (Figure S1H). Input from C-LTMRs and nociceptors were sparse (Figures S1E–S1G). To label PSDCs, we generated a genetic intersection targeting dorsal horn spinal neurons (Figure S1I), revealing that PSDCs project to both the Gr core and shell (Figure 1D).

Descending cortical projections reduce sensory transmission in the Cu,[42,43] but less is known about their role in the Gr. Using $Emx1^{Cre}$;$Rosa26^{LSL\text{-}Synaptophysin\text{-}TdTomato}$(Ai34) mice (Figure S2A) we identified cortical projections targeting both the Gr core and shell (Figure S2B). To investigate the origin of these projections, we performed viral injections into the somatosensory cortex (Figure S2C), focused either to M1, S1-forelimb (S1-FL) or S1-hindlimb (S1-HL) (Figures S2D–S2F). M1 injections resulted in sparse labeling in the Gr (Figure S2D). S1-FL projections labeled the Cu (Figure S2E), whereas S1-HL projections labeled the Gr core and shell (Figure S2F). Therefore, altered S1 signaling (specifically S1-HL), during pathological conditions[71–74] could disrupt tactile signaling within the Gr and contribute to aberrant tactile coding and pain.[75,76]

The cytoarchitecture of the Gr comprises VPL-PNs and local inhibitory interneurons

Within the DCN, feedforward and feedback inhibition modulate Gr projection neurons.[37,43,77–80] To characterize excitatory and inhibitory populations in the Gr, we used *in situ* hybridization to label $vGluT2^+$ excitatory neurons and $vGAT^+$ or $GlyT2^+$ inhibitory neurons (Figure 1E). The Gr core was enriched in excitatory neurons (Figure 1F), whereas the shell contained a more balanced excitatory-inhibitory distribution (Figure 1G). VPL-PNs

are the most prominent cell type in the DCN.[68] To characterize VPL-PNs in the context of local inhibition, we used viral retrograde tracing from the thalamus (Figure 1H) to fluorescently label VPL-PNs (Figure 1I) and a genetic mouse line (*Gad2*^{mCherry}) to visualize inhibitory neurons with a nuclear-localized reporter (Figure 1J). Inhibitory neurons were intermingled with VPL-PNs in the core (Figure 1K), but they were densely populated in the shell, where VPL-PNs were sparse (Figure 1L). Therefore, the Gr consists of a mixed excitatory/inhibitory core surrounded by an inhibitory shell.

Juxtacellular recordings in the Gr suggest that VPL-PNs are spontaneously active and cannot entrain to high-frequency stimulation, while Gr inhibitory neurons are not spontaneously active but can entrain to high frequencies.[37] To explore the physiological properties of Gr neurons, we performed slice electrophysiology (Figure 2A). VPL-PNs were more than twice as likely to exhibit spontaneous action potential (sAP) discharge than inhibitory neurons (Figures 2B and 2C). Of the spontaneously active neurons, VPL-PNs exhibited a higher sAP frequency than inhibitory neurons (Figure 2D), indicating greater baseline activity. VPL-PNs also showed increased excitability in response to small depolarizing currents, whereas inhibitory neurons exhibited greater firing rates at higher current amplitudes (Figures 2E and 2F). Additionally, VPL-PNs had a lower rheobase (Figure 2G) and a more hyperpolarized AP threshold (Figure 2H). When comparing other AP characteristics, we found no difference in the latency to threshold AP, AP rise time, afterhyperpolarization (AHP) amplitude, or AHP width (Table S1). We did, however, find that VPL-PNs exhibit larger AP amplitude, shorter AP width, and faster AP decay time (Table S1). Lastly, we observed that inhibitory neurons become more depolarized across current injection steps (Figure 2E). When comparing AP characteristics, we found that inhibitory neurons exhibited more adaptation in AP amplitude and AP threshold (Table S1). Finally, we found that VPL-PNs and inhibitory neurons share similar resting membrane potentials, while VPL-PNs exhibit a lower input resistance (Table S1).

Given the distinct intrinsic properties of VPL-PNs and inhibitory neurons, we compared excitatory synaptic input to each population by recording spontaneous excitatory postsynaptic currents (sEPSCs) (Figures 2I and 2J). A comparison of VPL-PNs and inhibitory neurons showed higher sEPSC frequency (Figure 2K) and larger sEPSC amplitude (Figure 2L) than VPL-PNs, with no differences in sEPSC kinetics (Figures 2M and 2N). These data indicate that Gr VPL-PNs supply sustained excitatory input to the VPL, while Gr inhibitory neurons are less likely to be spontaneously active and are likely more reliant upon ascending input. Interestingly, Gr VPL-PNs exhibited more excitable properties than Gr inhibitory neurons, suggesting sensory-evoked VPL-PN recruitment would precede inhibitory neuron recruitment and favor signal transmission to the VPL.

Gr VPL-PNs and inhibitory neurons are differentially innervated by primary afferent and spinal inputs

Recent work suggests that primary afferents and PSDCs converge onto Gr VPL-PNs.[37] However, the relative strengths of these two pathways onto VPL-PNs and inhibitory neurons is not well characterized. We next utilized slice electrophysiology to examine primary afferent and spinal inputs onto Gr VPL-PNs and inhibitory neurons. To characterize primary

afferent input onto Gr neurons, we generated *Advillin*^{Cre};*Rosa26*$^{LSL\text{-}ChR2/eYFP}$(Ai32) mice, where channelrhodopsin (ChR) was restricted to primary afferent terminals, and performed viral labeling of VPL-PNs, or generated *Advillin*^{Cre};Ai32;*Gad2*^{Cherry} mice, where inhibitory neurons were fluorescently labeled (Figure 3A). Similarly for PSDCs, we generated *Cdx2*^{Cre};*Lbx1*^{FlpO};*Rosa26*$^{CatCh/eYFP}$(Ai80) mice to express ChR in spinal projections, and performed viral labeling of VPL-PNs, or generated *Cdx2*^{Cre};*Lbx1*^{FlpO};Ai80;*Gad2*^{Cherry} mice, where inhibitory neurons were fluorescently labeled (Figure 3A). We found that primary afferents provide stronger excitatory input to both VPL-PNs and inhibitory neurons than PSDCs. Optical stimulation of primary afferents elicited robust monosynaptic EPSCs (Figures 3B–3D) and higher incidences of AP discharge in both VPL-PNs and inhibitory neurons (Figures 3E and 3F), with VPL-PNs receiving larger inputs than inhibitory neurons (Figure 3C). Despite pharmacological confirmation of monosynaptic transmission, latency and jitter of evoked-EPSCs were shorter in VPL-PNs (Figures S3A–S3E), suggesting input summation or closer prox- imity to primary afferent terminals (Figure S3F).

Notably, primary afferent and PSDC stimulation often induced a pause in sAP discharge, suggesting a feedforward inhibitory circuit (Figure 3G). This was confirmed by the presence of longer-latency inhibitory currents (Figure 3H), which were more prevalent in VPL-PNs than in inhibitory neurons (Figure 3I), suggesting that inhibitory neurons preferentially target the Gr core. After identifying a prominent feedforward inhibition of VPL-PNs, we sought to determine the functional connectivity between inhibitory neurons and VPL-PNs. We generated *Vgat*$^{IRES\text{-}Cre}$;Ai32 mice, where ChR was restricted to GABAergic and glycinergic inhibitory neurons, and performed viral labeling of VPL-PNs (Figure 3J). We observed optically evoked monosynaptic inhibitory postsynaptic currents (oIPSCs) in all VPL-PN recordings (Figure 3K). Pharmacological analysis indicated that inhibition was predominantly glycinergic, with a lesser contribution from GABAergic signaling (Figures 3K and 3L). Interestingly, both blockers had a larger impact of oIPSC amplitude when applied sequentially following the application of the other, suggesting a potential role for local disinhibition (pre- or postsynaptic) capable of modulating the direct inhibition of VPL-PNs. Despite this potential disinhibitory circuit, optogenetic activation of inhibitory neurons robustly inhibited VPL-PN sAP discharge, highlighting the potential of local inhibitory circuits to reduce VPL-PN output (Figure 3M). Additionally, VPL-PNs received robust glycine-dominant spontaneous inhibitory input (sIPSCs) (Figures 3N–3R).

Presynaptic inhibition in the DCN has been implicated in sensory-induced surround inhibition,[80] yet the organization of presynaptic inhibition in the DCN is not well characterized. Using vGAT immunolabeling, we identified putative inhibitory axoaxonic contacts[6,61,81] onto genetically labeled primary afferent (Figure S4A) and cortical terminals (Figure S4B) in the Gr. More primary afferent terminals received axoaxonic contacts than cortical afferent (Figure S4C), and primary afferents had more contacts per terminal (Figure S4D), consistent with the spinal dorsal horn.[61] To see whether this was conserved across species, we performed immunostaining in the macaques, where vGAT^{+} terminals (putative inhibitory contacts) were apposed to vGLUT1^{+} (presumed primary afferent terminals) (Figure S4E), suggestive of presynaptic contacts. Therefore, presynaptic inhibition in the Gr may mirror spinal inhibition following nerve injury[44,48] to facilitate tactile hypersensitivity.

In summary, these results reveal that primary afferents and PSDCs converge onto both VPL-PNs and inhibitory neurons, with primary afferents playing a dominant role. A robust feedforward inhibitory circuit shapes VPL-PN activity, underscoring the intricate interplay between excitatory and inhibitory circuits within the Gr.

Manipulation of Gr VPL-PNs and inhibitory neurons bidirectionally scales tactile sensitivity and intensity of withdrawal response to innocuous tactile stimuli

Lesions of the dorsal columns or DCN result in deficits such as impaired two-point discrimination[82–85] and reduced mechanical allodynia.[18,86] However, tactile sensation is spared post-lesion, presumably through a redundant pathway via the anterolateral tract.[82,87,88] Therefore, the extent and specificity of DCN contributions to tactile perception are not well characterized. Within the spinal cord, inhibition plays a critical role in setting pain thresholds,[57] and preventing innocuous information from engaging nociceptive pathways.[49,89] However, similar gating mechanisms are unlikely in the DCN given the absence of major nociceptive outputs. Interestingly, dorsal horn circuits exhibit intensity coding, where the strength of afferent activation determines whether a stimulus is interpreted as itch or pain.[90] We therefore explored whether similar intensity coding in the DCN contributes to tactile-evoked features of neuropathic pain.

Both VPL-PNs and inhibitory neurons in the Gr receive tactile input (Figures 3B–3F), making them likely contributors to tactile processing. To investigate VPL-PN function, we chemogenetically silenced Gr VPL-PNs (Figures 4A and 4B). Clozapine N-oxide (CNO) administration decreased tactile sensitivity to lower- and mid-force von Frey (VF) filaments (0.4–1.0 g), but it did not affect responses to higher forces (1.4–4 g) (Figure 4C). Additionally, CNO reduced sensitivity to dynamic brush stimulation (Figure 4D), but it had no effect on noxious mechanical pinprick (Figure S5B) or radiant heat sensitivity (Figure S5C). Collectively, these results suggest that VPL-PNs mediate responses to low-threshold, innocuous stimuli but not to noxious mechanical or thermal stimuli.

Blocking spinal inhibition generates exaggerated responses to tactile stimuli, resembling mechanical allodynia.[93] Given the robust inhibitory control of VPL-PN activity observed electro-physiologically (Figures 3G–3N), we next explored the functional role of Gr inhibition by chemogenetically silencing Gr inhibitory neurons (Figures 4E and 4F). CNO administration induced tactile hypersensitivity to lower-force VF filaments, similar to the heightened sensitivity seen in mice following spared nerve injury (SNI) models of neuropathic pain (Figure 4G). Silencing Gr inhibition also enhanced responses to dynamic brush (Figure 4H). Similar to VPL-PN manipulation, silencing Gr inhibition did not affect noxious mechanical pinprick (Figure S5E) or radiant heat sensitivity (Figure S5F). Importantly, we controlled for off-target effects of CNO (Figures S5G and S5H) and found no significant effects of CNO on VF (Figure S5I), dynamic brush (Figure S5J), pinprick (Figure S5K), Hargreaves (Figure S5L), or place preference (Figure S5M). Collectively, these results suggest that disrupting Gr inhibition generates tactile hypersensitivity to mechanical low-threshold stimuli, but it does not affect noxious mechanical or thermal responses.

Although silencing Gr inhibition heightened sensitivity to tactile stimuli, it is unclear whether this represents pain. Manipulation of spinal inhibition produces exaggerated paw withdrawal, such as shaking and guarding, which mirror mechanical allodynia.[46,93–96] To investigate how neuropathic pain or silencing Gr inhibition alters paw-withdrawal responses, we utilized high-speed videography paired with machine learning to record and quantify paw withdrawal to different stimuli. We used DeepLabCut[97] for markerless pose estimation of the metatarsophalangeal joint (MTP) (Figure 4I) and utilized Pain Assessment at Withdrawal Speeds (PAWS[91]) to extract relevant features, including shaking and guarding behaviors indicative of pain.[91] First, we compared withdrawal responses to a 0.6 VF filament, a dynamic brush, or a pinprick in uninjured mice and mice with an SNI model of neuropathic pain.[98] SNI mice exhibited enhanced paw-withdrawal responses to innocuous (0.6 VF, brush) and noxious (pinprick) stimuli (Figure 4J; Table S2), representing both allodynia and hyperalgesia. Comparatively, reducing Gr inhibition enhanced responses to 0.6 VF and brush but not to pinprick (Figure 4J; Table S3), resembling allodynia but not hyperalgesia. Therefore, silencing Gr inhibitory neurons specifically enhances tactile responses to a level resembling allodynia during neuropathic pain.

Second, we used an unsupervised machine learning approach, B-SOiD,[92] which has been utilized to classify pain-related paw-withdrawal signatures.[99] We utilized MTP coordinates to extract relevant behavioral clusters of movements, including rapid shaking (Figure 4K). Both SNI and silencing Gr inhibition increased brush-evoked shaking, whereas only SNI increased pinprick-evoked shaking (Figure 4K), reinforcing the specificity of Gr manipulations to tactile stimuli.

Finally, we asked whether reducing Gr inhibition was intrinsically aversive in the absence of experimentally applied stimulation. Conditioned place preference testing revealed that silencing Gr inhibition was aversive, suggesting an affective pain component (Figure 4L).

In summary, chemogenetic silencing of Gr VPL-PNs reduced sensitivity to low-threshold mechanical stimuli, whereas silencing Gr inhibitory neurons increased mechanical sensitivity to low-threshold stimuli in a manner resembling SNI-induced mechanical allodynia. Gr manipulations did not affect noxious mechanical or thermal sensitivity. Additionally, silencing Gr inhibition resulted in paw-withdrawal signatures resembling SNI-induced mechanical allodynia and induced aversion, suggesting that DCN circuits contribute to both sensory and affective components of tactile allodynia.

Increased tactile-evoked activity and altered primary afferent drive onto Gr VPL-PNs during neuropathic pain

Reduction of DCN activity attenuates mechanical allodynia during neuropathic pain.[18,21] Therefore, we asked whether Gr activity is increased during neuropathic pain. We performed c-Fos immunohistochemistry to assess neuronal recruitment[24] to a hindpaw brush stimulation of glabrous skin in anesthetized mice. We observed more Fos^+ cells in the Gr of SNI mice compared to sham mice (Figures 5A and 5B), with a greater proportion of VPL-PNs being recruited than inhibitory neurons (Figures S6A–S6D). Notably, VPL-PNs and inhibitory neurons were non-overlapping. Next, we performed *in vivo* extracellular recordings in the Gr of anesthetized SNI mice (Figure 5C), recording the

activity of ipsilateral and contralateral Gr in response to dynamic brush of the corresponding hindpaw. Stimulation of the injured hindpaw resulted in significantly higher evoked spiking activity compared to contralateral hindpaw stimulation (Figure 5D), with no difference in spontaneous spiking activity (Figure 5E). Collectively, these data suggest that the Gr exhibits heightened responses to tactile stimuli during neuropathic pain. However, whether this increased Gr excitability is attributed to the recruitment of more neurons, increased responses of individual neurons, increased strength of tactile inputs, or increased excitability of VPL-PNs or Gr inhibitory neurons was unclear.

To determine whether this hyperactivity was due to intrinsic changes in excitability, we characterized the intrinsic properties of Gr VPL-PNs and inhibitory neurons but found no difference in their responsiveness to depolarizing step currents post-SNI (Figures S7A–S7C and S7H–S7P). We also examined the properties of the threshold AP in each population (Figures S7D–S7M and S7Q–S7Z) and found that VPL-PNs APs exhibit faster kinetics and that inhibitory neurons APs are unchanged following SNI. While changes to AP kinetics may influence downstream neurotransmitter release,[100] these data suggest unaltered intrinsic excitability of Gr neurons post-injury. Next, we examined the spontaneous activity and excitatory drive to Gr VPL-PNs or inhibitory neurons. In line with previous work,[22] following SNI, VPL-PNs exhibited increased spontaneous AP discharge frequency (Figures S8A–S8C) and increased frequency of sEPSCs without changes to amplitude or kinetics (Figures S8D–S8I). Conversely, inhibitory neurons displayed no changes in spontaneous AP discharge (Figures S8J–S8L), a reduction in sEPSC amplitude, and no changes in sEPSC frequency or kinetics (Figures S8M–S8R). These findings align with our earlier observations that the activity of VPL-PNs and inhibitory neurons is governed by distinct presynaptic circuitry (Figures 3B–3I). Increased excitatory drive to VPL-PNs, with reduced input to Gr inhibitory neurons, has the potential to shift the excitation/inhibition balance of the Gr toward a hyperexcitable state.

To explore the potential contribution of altered input from primary afferents or spinal projections to Gr hyperactivity, we conducted slice electrophysiology in sham or SNI mice, where primary afferent or spinal terminals were optogenetically activated while recording from Gr VPL-PNs or inhibitory neurons. In line with our c-Fos data, a greater proportion of VPL-PNs fired APs in response to primary afferent stimulation following SNI (24/38 neurons, 63%) than was observed in sham mice (20/40 neurons, 50%) (Figure 5G), indicating an increase in the number of VPL-PNs recruited. Intriguingly, we observed an increase in the latency (Figure 5I) and latency standard deviation (Figure 5J) of optically evoked APs post-SNI, alongside a reduction in the reliability of optically evoked APs (Figure 5K), and a reduction in the number of evoked APs per stimulus (Figure 5L). These data indicate a shift toward increased variability and decreased reliability of primary afferent transmission following nerve injury. In line with this, whole-cell recordings revealed a shift in primary afferent input to VPL-PNs from synchronous to asynchronous release following SNI (Figures 5M and 5N), accompanied by a reduction in monosynaptic optically evoked EPSC (oEPSC) amplitude (Figure 5O) and an increased paired-pulse ratio (reduced release probability) (Figures 5P and 5Q). These findings are aligned with synchronicity of release being reduced at low release probability synapses.[101] Further analysis revealed that these changes were specific to neurons receiving asynchronous primary afferent input (Figures

S9A–S9F), which exhibited larger charge transfer with higher variability than synchronous inputs (Figures S9G and S9H). These data indicate that asynchronous inputs with reduced amplitude, larger charge, and greater variability underlie the altered recruitment profile of VPL-PNs following SNI. Finally, in cells where both oEPSCs and sEPSCs were recorded, we found that changes in spontaneous excitatory drive were specific to neurons receiving asynchronous primary afferent input (Figures S9I–S9L).

In contrast to the changes observed in primary afferent to VPL-PN synapses, we found no changes in primary afferent to inhibitory neuron (Figures S10A–S10F), spinal projection to VPL-PNs (Figures S10G–S10L), or spinal projection to inhibitory neuron (Figures S10M–S10R) synapses following SNI. Interestingly, we observed a mild reduction in the incidence of primary afferent evoked inhibition onto VPL-PNs post-SNI (Figure S11B), which could reveal polysynaptic excitatory circuitry.[89] Nevertheless, inhibitory receptor antagonists failed to induce prolonged excitatory responses in VPL-PNs (Figure S11C), suggesting that reduced inhibitory input is unlikely to account for the observed changes. Additionally, no alterations were observed in sIPSCs recorded from VPL-PNs post-SNI (Figures S11D–S11K), and optogenetically evoked IPSCs exhibited increased amplitude post-injury, with no changes in GABA/glycine composition (Figures S11L–S11O). To investigate why primary afferent inputs are altered in VPL-PNs but remain unchanged in inhibitory neurons, we analyzed the two major primary afferent sub-populations targeting the Gr: Aβ RA- and Aβ Field-LTMRs (Figures S1A and S1B). Post-SNI, Aβ RA-LTMR inputs to VPL-PNs were reduced, while Aβ Field-LTMR input remained stable (Figures S12A–S12F). In contrast, inhibitory neurons showed no change in Aβ RA-LTMR input (Figures S12G–S12J). Notably, Aβ RA- and Aβ Field-LTMRs input is predominantly localized to the gracile core, where VPL-PNs are situated (Figures S12K and S12L). Interestingly, microglial recruitment post-injury was similarly confined to the Gr core (Figures S12M and S12N). This spatial organization may explain why VPL-PNs are preferentially impacted in our slice experiments, whereas changes to inhibitory neuron recruitment could be driven by alternative mechanisms such as descending cortical control.[43]

In summary, neuropathic injury leads to increased c-Fos$^+$ expression and increased spiking activity in the Gr in response to tactile stimulation. Gr VPL-PNs exhibit increased recruitment in response to primary afferent activation, albeit with reduced reliability, and increased variability. We provide evidence that altered Gr signaling is at least in part due to a shift in primary afferent signaling from synchronous to asynchronous onto VPL-PNs.

Enhancing Gr inhibition alleviates tactile hypersensitivity and neuropathic pain-induced paw-withdrawal signatures

Blockade of DCN activity ameliorates tactile hypersensitivity during neuropathic pain.[18,21] However, the specific functional contributions of VPL-PNs and inhibitory neurons to tactile hypersensitivity is not well understood. Since Gr manipulations scale tactile responses in naive mice (Figures 4C and 4G) and can facilitate neuropathic pain-like paw-withdrawal features (Figures 4I–4K), we hypothesized that inhibition of Gr VPL-PNs or activation of Gr inhibitory neurons during neuropathic pain would alleviate tactile allodynia.

Gr VPL-PNs display increased recruitment to electrical stimulation of a transected peripheral nerve,[24] yet their direct contribution to tactile hypersensitivity is not well characterized. To understand the functional contributions of VPL-PNs to neuropathic pain, we performed chemogenetic manipulation of VPL-PNs following SNI (Figures 6A and 6B). SNI mice developed the expected punctate tactile hypersensitivity compared to naive mice, which was partially alleviated by the administration of CNO (Figure 6C). CNO did not affect responses to dynamic brush (Figure 6D), pinprick (Figure S13B), or Hargreaves (Figure S13C), and did not induce place preference (Figure S13D). Therefore, chemogenetic inhibition of VPL-PNs selectively and partially reduced tactile hypersensitivity during neuropathic pain.

Enhancing inhibition in the spinal cord alleviates symptoms of neuropathic pain.[65,102–106] Inhibition in the DCN is suggested to become impaired during neuropathic pain,[29] which may contribute to neuropathic pain-like behaviors observed after silencing inhibition in the Gr (Figures 4E–4L). To test whether enhancing Gr inhibition could ameliorate tactile allodynia during neuropathic pain, we optogenetically activated Gr inhibitory neurons in SNI mice (Figures 6E and 6F). Given the effectiveness of multiple activation paradigms,[107–110] we first provided either a 20-Hz stimulation or continuous stimulation using 470-nm blue light to activate ChR2.[111–114] Stimulation at 20 Hz was less effective at reducing tactile hypersensitivity than constant blue light (Figure 6G). Thus, we utilized continuous blue light for subsequent experiments and orange light as a control for wave-length-independent heating during optical stimulation.[115] Blue or orange light stimulation did not reduce mechanical allodynia in response to brush (Figure 6H), mechanical hyperalgesia induced by a pinprick (Figure S13F), or thermal hyperalgesia by Hargreaves (Figure S13G). We repeated these experiments in a clinically relevant chemotherapy-induced model of peripheral neuropathy (CIPN).[116–118] Similar to SNI, blue light stimulation in CIPN mice reduced tactile hypersensitivity to VF (Figure 6I), but did not affect response to brush (Figure 6J), pinprick (Figure S13H), or Hargreaves (Figure S13I). Collectively, activation of Gr inhibition specifically reduced punctate tactile hypersensitivity to lower threshold VF stimuli during multiple neuropathic pain models.

We next investigated whether activating Gr inhibition could alleviate affective pain following SNI or CIPN. We once again used PAWS to track the paw-withdrawal response to innocuous or noxious mechanical stimuli to identify shaking and guarding behavior (Figure 7A). In SNI mice, optogenetic stimulation of Gr inhibition reduced distance traveled, shaking, and velocity in response to tactile stimuli but not for noxious pinprick (Figure 7B; Table S4). Next, we utilized B-SOiD as an unsupervised approach to investigate whether shaking in SNI mice was reduced by activating Gr inhibition. We found that the previously identified shaking module (Figure 4K) had reduced usage when activating Gr inhibition (Figure 7C). Lastly, we determined whether activating Gr inhibition was sufficient to induce place preference, suggestive of an analgesic effect.[119] Interestingly, while SNI mice did not display a real-time place preference, they did display preference for the stimulated side 1 h following the final conditioning trial (Figure 7D).

Similar to SNI, CIPN mice showed reduced intensity of paw-withdrawal responses to 0.6-VF and brush stimuli when activating Gr inhibition but no change to pinprick as measured

by PAWS (Figures 7E and 7F; Table S5) and B-SOiD (Figure 7G). CIPN mice also did not display a real-time place preference to activation of Gr inhibitory neurons, but they did display a preference 1 and 24 h post-conditioning (Figure 7H).

In summary, reducing Gr VPL-PN activity or activating Gr inhibition during neuropathic pain reduces tactile hypersensitivity and allodynia but not hyperalgesia. Additionally, activation of Gr inhibition reduced pain-associated paw-withdrawal responses to normally innocuous stimuli and induced a place preference associated with pain relief in both SNI and CIPN mice.

DISCUSSION

In this study, we found Gr VPL-PNs and are differentially innervated by primary afferents and spinal projections. Functional manipulations of either Gr population scaled tactile sensitivity; inhibition of Gr VPL-PNs reduced mechanical sensitivity to low-threshold VF stimuli, while inhibition of Gr inhibitory neurons increased tactile sensitivity and generated paw-withdrawal signatures that resembled neuropathic mice. In nerve-injured mice, we found enhanced tactile-evoked activity coupled with altered excitatory drive from primary afferents onto VPL-PNs. Optogenetic activation of Gr inhibition alleviated tactile allodynia and reduced paw-withdrawal features associated with neuropathic pain. These results suggest that manipulation of Gr circuits can scale tactile responses in naive and neuropathic conditions, representing a key pathway mediating tactile allodynia.

Gr circuits promote VPL-PN signal transduction modulated by sensory-driven feedforward inhibition

Slice electrophysiology revealed stronger inputs from primary afferents onto VPL-PNs compared to spinal projections, consistent with anatomical observations. Gr inhibitory neurons displayed a similar predominance of primary afferent input over spinal, suggesting that tactile responses in the Gr are largely driven by the direct DRG pathway. However, VPL-PNs receive stronger inputs from both primary afferents and spinal projections compared to inhibitory neurons, suggesting that sensory-driven activity in the Gr would predominantly activate VPL-PNs followed by inhibition. VPL-PNs were more spontaneously active than inhibitory neurons, consistent with work suggesting that Gr VPL-PNs have stronger intensity encoding than Gr inhibitory neurons.[37] Therefore, VPL-PNs transmit both spontaneous and sensory-evoked activity to the VPL, while inhibitory neurons are likely to be more dependent on sensory-driven activation. Inhibitory neurons favor the core, supporting the idea of sensory-drive feedforward[39] and surround inhibition of VPL-PNs[37] in the Gr. Additionally, Gr cortical projections may mirror those in the Cu, which enable tactile feedback modulation,[43] to alter hindlimb tactile coding.

The Gr selectively scales tactile sensitivity

Manipulations of either Gr VPL-PNs or Gr inhibitory neurons specifically altered tactile sensitivity and paw-withdrawal responses to tactile stimuli, but they did not affect noxious mechanical and thermal sensitivity or withdrawal responses to noxious mechanical stimuli. Consistent with this, responses to noxious pinprick or heat are mediated by

spinal reflex circuits,[120,121] while spinal cord lamina I projection neurons transmit nociceptive information for pain perception.[56,122] Therefore, Gr manipulations do not affect anatomically distinct nociceptive pathways. During neuropathic pain, silencing VPL-PNs or activating Gr inhibition reduced tactile hypersensitivity, but they did not affect noxious mechanical or thermal hypersensitivity. Additionally, activating Gr inhibition reduced pain-associated paw-withdrawal signatures to tactile but not noxious stimuli. These results are consistent with increasing spinal inhibition to treat chronic pain,[65,104–106] although Gr manipulations were specific to tactile stimuli. These results also match other Gr manipulations, including lidocaine administration into the Gr,[18] dorsal column lesions following nerve injury,[21] or spinal hemisection,[123] which do not affect thermal responses. These results are relevant for maladaptive tactile chronic pain manifestations while leaving acute protective pain unaffected.

Increased recruitment and altered tactile coding in Gr following nerve injury

Following nerve injury, enhanced Gr activity is associated with neuropathic pain.[22,24] Supporting this, c-Fos labeling and *in vivo* extracellular recordings show enhanced tactile-evoked neuronal recruitment and spiking activity following nerve injury. Additionally, prolonged asynchronous primary afferent signaling engaged more neurons and promoted an increase in the latency to and variability of VPL-PN activation, resembling the dorsal horn after injury.[124] Consistent with our findings of increased spontaneous discharge in and increased excitatory drive onto VPL-PNs, Aβ-LTMR stimulation and sensory-evoked afterdischarge have been reported in Gr VPL-PNs following nerve injury.[22] This increased background activity, coupled with altered signal reliability and reduced synchronicity could introduce signal noise and lower the temporal fidelity of tactile signaling. Given the known role of the DCN in tactile discrimination,[16] such changes could contribute to altered tactile acuity in chronic pain states.[125]

Despite increased sensory-evoked c-Fos expression in both VPL-PNs and inhibitory neurons, slice electrophysiology revealed altered signaling exclusively in VPL-PNs. We propose two primary explanations. (1) Injury-impacted primary afferent inputs are predominantly localized to the Gr core, where VPL-PNs are concentrated, while inhibitory neurons are predominantly in the Gr shell. Therefore, it is likely that injury-induced plasticity driven by mechanisms such as microglia[126–129] preferentially impacts VPL-PNs. Specific reduction of putative Aβ RA-LTMR inputs onto VPL-PNs after SNI suggests that further investigation of DRG subtypes may reveal more intricate plasticity following neuropathic injury. (2) Descending control of inhibitory neurons: similar to that reported in the present study, Cu inhibitory neurons are critical regulators of VPL-PN activity and are modulated by cortical inputs.[43] Previous studies have reported cortical hyperexcitability following neuropathic injury,[72,130–132] suggesting enhanced S1-HL drive post-injury could play an important role in shaping Gr inhibitory neuron activity *in vivo*.

Although we did not reveal changes to PSDC synaptic signaling, our reduced preparation cannot fully rule out alterations in PSDC excitability or their synaptic inputs. Recently, the DCN→ VPL pathway was suggested to transmit high-force information coming from PSDCs.[37] However, little is currently known about how PSDCs are impacted by neuropathic

injury. It is plausible that PSDCs could exhibit increased excitatory drive or gain access to additional afferent inputs through mechanisms such as spinal disinhibition following nerve injury. Investigating potential alterations in PSDC recruitment and its effects on amplified DCN signaling during chronic pain would be of great interest.

Allodynia through tactile scaling in the DCN

Chemogenetic silencing of Gr inhibitory neurons elicited allodynia similar to impairing spinal inhibition.[93,96,133] In the spinal cord, reduced presynaptic inhibition[44] and postsynaptic inhibition contribute to neuropathic pain.[89,134] As a consequence, tactile information engages lamina I nociceptive circuits and facilitates allodynia.[6,7,135] However, this model of allodynia cannot be applied to the inherent tactile nature of DCN circuits. While we did observe a moderate reduction in sensory-evoked inhibition incidence, we found no changes in spontaneous inhibition or inhibitory transmission onto Gr VPL-PNs. Therefore, rather than “ungating” tactile information, enhanced DCN activity likely influences targets such as the VPL, which contains touch and nociception-responding neurons.[136] Additionally, PSDC-mediated high force activity in the DCN may be amplified during neuropathic pain.[37] DCN projections to the periaqueductal gray[137] and spinal cord[138] have also been described, suggesting alternate routes for tuning tactile and nociceptive information.

Redundant pathways for the modulation of neuropathic pain

Classical views suggest the anterolateral tract transmits noxious information,[139] while the dorsal columns transmit touch.[140] However, tactile perception is retained in dorsal column lesions when the anterolateral pathway is spared.[83] Additionally, the parabrachial nucleus receives both tactile and nociceptive information and is a key regulator of neuropathic pain.[8,9,141] These results suggest a more comprehensive model where converging streams of information across multiple pathways contribute to naive and neuropathic states. Supporting this, both spinothalamic and DCN projections target the same area of the VPL,[142] which receives convergent innocuous and noxious information. Importantly, the lateral thalamus exhibits plasticity following nerve injury[143] and is implicated in chronic pain processing.[144] Therefore, DCN-driven input following VPL neuroplasticity[75,143,145] may contribute to tactile-evoked pain perception.

Limitations of the study

In vivo extracellular recordings and c-Fos activity measurements were conducted in anesthetized mice, and anesthetics can significantly influence neural activity. Additionally, patch-clamp recordings were performed in a reduced acute slice preparation, which may not fully capture the complexities of neural activity in intact systems. Future recordings in awake, behaving animals would provide a more physiologically relevant assessment of Gr neural activity in response to sensory stimuli. Moreover, optogenetic approaches utilized in slice electrophysiology and behavior have inherent limitations. It is improbable that large populations of neurons are synchronously activated to the extent achieved by ChR2-mediated activation in physiological conditions. Additionally, continuous optogenetic stimulation during behavior is unlikely to mimic the physiological activation of inhibitory neurons.

RESOURCE AVAILABILITY

Lead contact

Requests for information and further resources should be directed to and will be fulfilled by the lead contact, Victoria E. Abraira (victoria.abraira@rutgers.edu).

Materials availability

This study did not generate new unique reagents.

Data and code availability

- All data reported in this paper will be shared by the lead contact upon request.
- This paper does not report original code.
- Any additional information required to reanalyze the data reported in this paper is available from the lead contact upon request.

STAR★METHODS

EXPERIMENTAL MODEL AND STUDY PARTICIPANT DETAILS

Mouse lines used to target DRG neuron populations include *Advillin*^{Cre} or *Advillin*^{FlpO} for all DRG neurons,[146,151] *Th*^{2aCreER} for C-LTMRs,[61] *Trkb*^{CreER} for Aδ-LTMRs,[152] *Ret*^{CreER} for Aβ RA-LTMRs,[69,149] *Trkc*^{CreER} for Aβ SA1-LTMRs,[153] *Ptgfr*^{CreER} for Aβ Field-LTMRs,[68] *Pvalb*^{2aCreER} for proprioceptors,[69] *Mrgprd*^{CreER} for nonpeptidergic nociceptors,[154] and *Trpv1*^{Cre} for peptidergic nociceptors.[155] Mouse lines used to target the spinal cord include *Cdx2*^{Cre} for CNS tissue below spinal segment C2,[156] and *Lbx1*^{FlpO} for dorsal horn neurons.[157] Mouse lines used to target inhibitory interneuron populations include *Vgat*$^{IRES\text{-}Cre}$ and *Gad2*^{Cherry} for GABAergic inhibitory neurons.[158,159] *Emx1*$^{IRES\text{-}Cre}$ and *Rbp4*^{Cre} were used to target cortical neurons.[148,160] For visualization or manipulation of Cre and/or Flp-dependent populations, we utilized the following mouse lines: *Rosa26*$^{LSL\text{-}FSF\text{-}tdTomato}$ (Ai65),[161] *Rosa26*$^{LSL\text{-}FSF\text{-}synaptophysin\text{-}GFP}$ (FPSit),[162] *Rosa*26$^{LSL–SynGFP}$ (LSL-SynGFP, derived from FPSit[162]), *Rosa26*^{LSL}-synaptophysin-tdTomato (Ai34), *Rosa26*$^{LSL–ChR2–YFP}$ (Ai32),[163] *Rosa26*$^{LSL–FSF\text{-}ChR2–YFP}$ (Ai80),[164] and *Tau*$^{ds\text{-}DTR}$ (DTR).[150] Transgenic mouse strains were used and maintained on a mixed genetic background (129/C57BL/6). Experimental animals used were of both sexes. With the exception of *in vivo* recordings, housing, surgery, behavioral experiments and euthanasia were performed in compliance with Rutgers University Institutional Animal Care and Use Committee (IACUC; protocol #201702589). All mice used in experiments were housed in a regular light cycle room (lights on from 08:00 to 20:00) with food and water available *ad libitum*. *in vivo* recordings were performed at the lab of Dr. Eiman Azim according to the Animal Care and Use Committee (IACUC; protocol #16–00011) at the Salk Institute. Cortical injections were performed at the lab of Dr. Yutaka Yoshida according to the Animal Care and Use Committee (IACUC; protocol #2018–0045) at the Burke Neurological Institute. All mice used in experiments were housed in a regular light cycle room (lights on from 07:00 to 19:00) with food and water available *ad libitum*.

METHOD DETAILS

Genetic crosses and statistical methods related to individual figures

Genetic crosses and statistical methods related to Figure 1: (A) Primary afferents were labeled using *Advillin*^{Cre} mice, where Cre expression is restricted to the DRG,[151] crossed with an *Rosa26*$^{LSL\text{-}Synaptophysin\text{-}GFP}$ mouse derived from the FPSit line,[162] which allows for Cre-dependent visualization of synaptic terminals. (B) Spinal afferents were labeled using a genetic intersection of *Cdx2*^{Cre}, where Cre expression was restricted to the caudal nervous system,[156] and the *Lbx1*^{FlpO} line, where Flp expression is restricted to the spinal dorsal horn.[157] These mice were crossed to the FPSit reporter line[162] to allow for Cre- and Flp-dependent visualization of spinal synaptic terminals. (F,G) Quantification of excitatory and inhibitory markers in the Gr core (F) and shell (G) normalized to total DAPI. The Gr core had a significantly higher number of VGlut2+ cells compared to vGAT+ or GlyT2+ cells. $N = 4$ mice per group, One-way ANOVA, Tukey's multiple comparisons, VGlut2 vs. VGAT $^{**}p = 0.0049$, VGlut2 vs. Glyt2 $^{**}p = 0.001$, VGAT vs. Glyt2 $p = 0.5127$. The Gr shell had a more even distribution of excitatory and inhibitory neurons. $N = 4$ mice per group, One-way ANOVA, Tukey's multiple comparisons, VGlut2 vs. VGAT $p = 0.9655$, VGlut2 vs. Glyt2 $p = 0.2565$, VGAT vs. Glyt2 $p = 0.3583$. Error bars represent SEM. (**K,L**) Quantification of Gr VPL-PNs and GAD2+ inhibitory neurons in the core (H) and shell (I). The Gr core had similar numbers of VPL-PNs and inhibitory neurons. $N = 3$ mice per group, unpaired t test, $p = 0.6502$. The Gr shell had significantly more inhibitory neurons than VPL-PNs. $N = 3$ mice per group, unpaired t test, $^{***}p = 0.0005$. Error bars represent SEM.

Statistical methods related to Figure 2: (A) To label VPL-PNs, we injected ~420 nL of pENN.AAV.CB7.CI.eGFP.WPRE.rBG (AAV9) into the VPL, and used *Gad2*^{Cherry} mice to visualize inhibitory neurons.[159] (C) Characterization of sAP incidence: $n = 91$ VPL-PNs from 9 mice, and $n = 82$ inhibitory neurons from 6 *Gad2*^{Cherry} mice. (D) Characterization of sAP discharge frequency: $n = 81$ VPL-PNs from 9 mice, and $n = 32$ inhibitory neurons from 6 *Gad2*^{Cherry} mice. VPL-PNs exhibit higher sAP discharge frequency: Mann-Whitney test, $^{****}p < 0.0001$. (**E-H**) Characterization of Gr VPL-PN and Gr inhibitory neurons response to depolarizing current injection: $n = 32$ VPL-PNs from 5 mice, and $n = 41$ inhibitory neurons from 6 *Gad2*^{Cherry} mice. (F) VPL-PNs fire more APs at 10 pA, 20 pA, and 30 pA current injection steps: Mixed-effects model with Geisser-Greenhouse correction and Sidak's multiple comparisons test, 10 pA $^{**}p = 0.0014$; 20 pA $^{**}p = 0.0024$; 30 pA $^{*}p = 0.0190$; 40 pA, $p = 0.0763$; 50 pA, $p = 0.3036$; 60 pA, $p = 0.8957$; 70 pA, $p = 0.9952$; 80pA, $p > 0.9999$; 90pA, $p > 0.9999$; 100pA, $p = 0.9997$; 110pA, $p = 0.9872$; 120pA, $p = 0.9114$. (G), lower rheobase: Mann-Whitney test, $^{**}p = 0.0026$ (**H**), and a more hyperpolarized AP threshold: Unpaired T test, $^{****}p < 0.0001$. (**K-N**) Characterization of sEPSCs: $n = 79$ VPL-PNs from 10 mice, and $n = 47$ inhibitory neurons from 7 *Gad2*^{Cherry} mice. (**K**) VPL-PNs receive higher frequency sEPSC input: Mann-Whitney test, $^{***}p = 0.0005$, (**L**) with larger amplitude: Mann-Whitney test, $^{****}p < 0.0001$, (**M**) similar rise time: Mann-Whitney test, $p = 0.4038$, (**N**) and similar decay: Mann-Whitney test, $p = 0.2976$.

Genetic crosses and statistical methods related to Figure 3: (A) To activate primary afferent inputs onto VPL-PNs, we generated *Advillin*^{Cre};*Rosa26*$^{LSL–ChR2–YFP}$(Ai32)[163] mice, where ChR2 expression was restricted to primary afferent terminals, and injected ~420 nL of pENN.AAV.CB7.CI.mCherry.WPRE.RBG into the VPL to visualize Gr VPL-PNs. To activate spinal inputs onto VPL-PNs, we generated *Cdx2*^{Cre};*Lbx1*^{FlpO};*Rosa26*$^{LSL–FSF-CatCh-eYFP}$(Ai80)[165] mice, where a calcium translocating channelrhodopsin (CatCh) was expressed in spinal afferent terminals in the Gr, and injected ~420 nL of pENN.AAV.CB7.CI.mCherry.WPRE.RBG into the VPL. To activate primary afferent or spinal inputs onto Gr inhibitory neurons, we generated *AdvillinCre*;Ai32;*Gad2*^{Cherry} mice to activate primary afferents or *Cdx2*^{Cre};*Lbx1*^{FlpO};Ai80;*Gad2*^{Cherry} mice to activate spinal inputs onto fluorescently labeled inhibitory neurons.[159] (C) Amplitude of monosynaptic responses to photostimulation of primary afferent terminals (*Advillin*^{Cre};Ai32) recorded in 41 VPL-PNs from 7 mice; 44 inhibitory neurons from 6 mice, and spinal projection terminals (Cdx2^{Cre};Lbx1^{FlpO};Ai80) recorded in 51 VPL-PNs from 6 mice; 14 inhibitory neurons from 3 mice. VPL-PNs receive larger input than inhibitory neurons from primary afferents: Mann-Whitney test, ****$p < 0.0001$, and spinal projections: Mann-Whitney test, ***$p = 0.0004$. (**J**) To activate inhibitory inputs onto VPL-PNs, we generated *Vgat*$^{IRES-Cre}$;*Rosa26*$^{LSL–ChR2–YFP}$(Ai32)[163] mice, where ChR2 expression was restricted to inhibitory terminals, and injected ~420 nL of pENN.AAV.CB7.CI.mCherry.WPRE.RBG into the VPL to visualize Gr VPL-PNs. (**K-L**) Optically-evoked IPSCs were recorded from 34 VPL-PNs in 6 mice. Bicuculline (10 μM) was applied first in 6 recordings, strychnine (1 μM) was applied first in 7 recordings, and bicuculline and strychnine were sequentially applied in 11 recordings from 5 mice. One-Way ANOVA with Dunnett's multiple comparisons test: Control vs. Bic, $p = 0.4456$, Control vs. Strych, ****$p < 0.0001$, Control vs. BS, ****$p < 0.0001$. (**N-R**) Spontaneous IPSCs were recorded from 32 VPL-PNs in 6 mice. Bicuculline (10 μM) was applied first in 6 recordings, strychnine (1 μM) was applied first in 8 recordings, and bicuculline and strychnine were sequentially applied in 9 recordings from 6 mice. (**O**) Normalized sIPSC Frequency: Kruskal-Wallis with Dunn's multiple comparisons test; Control vs. Bic, $p = 0.2388$, Control vs. Strych, **$p = 0.0056$, Control vs. BS, ****$p < 0.0001$. (**P**) Normalized sIPSC amplitude: Kruskal-Wallis with Dunn's multiple comparisons test; Control vs. Bic, **$p = 0.0078$, Control vs. Strych, ****$p < 0.0001$. (**R**) Normalized sIPSC Decay: One-way ANOVA with Dunnett's multiple comparisons test, with single pooled variance; Control vs. Bic, $p = 0.0538$, Control vs. Strych, ****$p < 0.0001$.

Statistical methods related to Figure 4: (A,B) To restrict DREADD expression to VPL-PNs we injected a retrograde Cre-virus (pENN.AAV.hSyn.Cre.WPRE.hGH AAVrg) into the VPL, and injected a Cre-dependent hM4Di DREADD virus (pAAV1-hSyn-DIO-hM4D(Gi)-mCherry AAV1) into the Gr. (C) CNO-treated mice exhibited a decreased tactile sensitivity to von Frey filaments compared to saline-treated mice. $N = 12$ mice, two-way ANOVA with repeated measures, Sidak's multiple comparisons, 0.4 VF ***$p = 0.0008$, 0.6 VF *$p = 0.0101$, 1 VF *$p = 0.0346$. Error bars represent SEM. (D) CNO mice exhibited a decreased average brush score compared to saline mice. $N = 12$ mice, Wilcoxon test, *$p = 0.0469$. (E,F) To restrict DREADD expression to Gr inhibitory neurons, we injected a Cre-dependent hM4Di DREADD virus (pAAV1-hSyn-DIO-hM4D(Gi)-mCherry) into the Gr of *Vgat*$^{IRES-Cre}$ mice. (G) CNO-treated mice and SNI mice had significantly increased von

Frey sensitivity compared to saline controls. $N = 8$ mice, two-way ANOVA with repeated measures, Tukey's multiple comparisons, * = CNO vs. Saline, 0.04 VF ***$p = 0.0002$, 0.07 VF **$p = 0.0039$, 0.16 VF *$p = 0.0148$, 0.4 VF ***$p = 0.0001$, # = SNI vs. Saline, 0.008 VF $^{\#}p = 0.0266$, 0.04 VF $^{\#\#}p = 0.0011$, 0.07 VF $^{\#}p = 0.0336$, 0.16 VF $^{\#\#\#}p = 0.0005$, 0.4 VF $^{\#\#}p = 0.0039$, 0.6 VF $^{\#\#}p = 0.0062$. Error bars represent SEM. (**H**) CNO mice had significantly increased average brush score compared to saline mice. $N = 8$ mice, Wilcoxon test, *$p = 0.0156$. (**J**) Comparison of PAWS features of SNI or CNO mice compared to saline controls. $N = 16$ mice, symbols indicate how parameters change after either SNI or chemogenetic manipulation compared to control: ↑ = increase, ↓ = decrease, - = no change. ↑ = $p < .05$, ↑↑ = $p < .005$. See Tables S2 and S3 for statistics. (**K**) Usage of the shaking module by SNI and CNO mice compared to saline controls. $N = 23$ mice (23 saline videos, 16 CNO videos, and 15 SNI videos), Kruskal-Wallis test, Dunn's multiple comparisons. There were no differences amongst groups in response to a 0.6 VF stimulus. Saline vs. CNO $p = 0.491$, Saline vs. SNI $p = 0.0825$, CNO vs. SNI $p > 0.9999$. CNO and SNI mice had increased shaking in response to brush stimuli compared to controls. Saline vs. CNO **$p = 0.0014$, Saline vs. SNI ***$p = 0.0003$, CNO vs. SNI $p > 0.9999$. In response to a noxious pinprick, SNI mice had a significantly increased usage compared to saline and CNO mice. Saline vs. CNO $p > 0.9999$, Saline vs. SNI *$p = 0.0174$, CNO vs. SNI *$p = 0.0215$. (**L**) Chemogenetic silencing of Gr inhibitory neurons induced a conditioned place aversion. $N = 8$ mice, paired t test, **$p = 0.003$.

Statistical methods related to Figure 5: (B) Brush stimulation of SNI mice resulted in a significant increase in the number of c-Fos+ cells in the Gr compared to sham controls. $N = 4$ mice per group, Mann-Whitney test, *$p = 0.0286$. (D) Evoked Gr spiking activity on the hindpaw ipsilateral to SNI was significantly increased compared to stimulation on the contralateral uninjured side. $N = 5$ mice, paired t test, **$p = 0.0048$. (E) Spontaneous Gr spiking activity was not significantly different between ipsilateral and contralateral sides. $N = 5$ mice, paired t test, $p = 0.7773$. (**F-P**) Strategy to investigate primary afferent inputs onto VPL-PNs is the same as Figure 3A, with the addition of the SNI procedure to induce neuropathic pain. (**G-L**) Primary afferent-evoked AP discharge was recorded in 40 VPL-PNs from 5 sham mice and 38 VPL-PNs from 4 SNI mice. SNI mice exhibited (**I**) increased latency to the first oAP: Mann-Whitney test, **$p = 0.0040$, (**J**) first oAP latency SD: Mann-Whitney test, **$p = 0.0056$, and (**K**) reduced oAP reliability: Mann-Whitney test, *$p = 0.0182$, and (L) average oAP number per stimulus: Mann-Whitney test, *$p = 0.0336$. (**M-O**) Primary afferent-evoked EPSCs were recorded in 41 VPL-PNs from 7 sham mice and 36 VPL-PNs from 4 SNI mice. (**O**) We found reduced monosynaptic oEPSC amplitude following SNI: Mann-Whitney test, *$p = 0.00490$. (**P**) Paired-pulse ratio was examined in 21 VPL-PNs from 4 sham mice and 29 VPL-PNs from 4 SNI mice. SNI exhibited reduced paired-pulse ratio: Unpaired t test, **$p = 0.0076$.

Statistical methods related to Figure 6: (A,B) To restrict DREADD expression to VPL-PNs we injected a retrograde Cre-virus (pENN.AAV.hSyn.Cre.WPRE.hGH AAVrg) into the VPL, and injected a Cre-dependent hM4Di DREADD virus (pAAV1-hSyn-DIO-hM4D(Gi)-mCherry AAV1) into the Gr, after which mice received an SNI procedure to induce neuropathic pain. (C) SNI mice developed hypersensitivity to von Frey stimulation

compared to uninjured mice, which was partially rescued by chemogenetic inhibition of VPL-PNs. N = 12 mice, two-way ANOVA with repeated measures, Tukey's multiple comparisons, * = Uninjured+Saline vs. SNI+Saline, 0.008 VF *p = 0.0174, 0.04 VF ****p < 0.0001,.0.07 VF ****p < .0.0001, 0.16 VF ****p < .0.0001, 0.4 VF ***p = 0.0002, 0.6 VF ***p = 0.0001. $^{\#}$ = SNI+Saline vs. SNI+CNO, 0.04 VF $^{\#\#\#}p$ = 0.0004, 0.07 VF $^{\#\#\#}p$ = 0.0003, 0.16 VF $^{\#\#\#}p$ = 0.0001, 0.4 VF $^{\#\#}p$ = 0.0041. † = Uninjured+Saline vs. SNI+CNO, 0.6 VF $^{\dagger\dagger}p$ = 0.0014. (D) Chemogenetic inhibition of VPL-PNs following SNI did not significantly affect average brush score compared to saline-treated mice. N = 12 mice, Wilcoxon test, p = 0.5688. (E,F) We generated *Vgat*$^{IRES\text{-}Cre}$;Ai32 mice to optogenetically activate inhibitory terminals in the Gr. (G) Optogenetic activation of Gr inhibition using continuous blue light stimulation was more effective than 20 Hz blue light stimulation at reducing hypersensitivity to von Frey stimulation in SNI mice compared to a control continuous orange light stimulation. N = 10 mice, two-way ANOVA with repeated measures, Tukey's multiple comparisons. * = Orange cont vs. Blue cont, 0.008 VF **p = 0.001, 0.02 VF ****p < 0.0001, 0.04 VF ***p = 0.0002, 0.07 VF ****p < 0.0001, 0.16 VF ****p < 0.0001. $^{\#}$ = Orange cont vs. Blue 20Hz, 0.008 VF $^{\#\#}p$ = 0.0047, 0.02 VF $^{\#\#\#}p$ = 0.001, 0.04 VF $^{\#\#\#}p$ = 0.005, 0.07 VF $^{\#\#}p$ = 0.004, 0.16 VF $^{\#}p$ = 0.0109. † = Blue cont vs. Blue 20Hz, 0.07 VF $^{\dagger\dagger\dagger}p$ = 0.0009, 0.16 VF $^{\dagger}p$ = 0.0255, 0.4 VF $^{\dagger}p$ = 0.0221. (**H**) Blue light stimulation did not significantly affect average brush score compared to orange light stimulation in SNI mice. N = 8 mice, Wilcoxon test, p = 0.1563. (**I**) Optogenetic activation of Gr inhibition using continuous blue light reduced hypersensitivity to von Frey stimulation in CIPN mice compared to a control continuous orange light stimulation. N = 10 mice, two-way ANOVA with repeated measures, Sidak's multiple comparisons, 0.008 VF *p = 0.0105, 0.02 VF **p = 0.0079, 0.04 VF **p = 0.0015, 0.07 VF *p = 0.0115, 0.16 VF ****p < 0.0001, 0.4 VF ***p = 0.0009. (**J**) Blue light stimulation did not significantly affect average brush score compared to orange light stimulation in CIPN mice. N = 10 mice, Wilcoxon test, p = 0.75.

Statistical methods related to Figure 7: (B) Comparison of PAWS features of blue light stimulation versus orange light stimulation in SNI mice. ↑ = increase, ↓ = decrease, - = no change. ↓ = p < .05. See Table S4 for statistics. (C) Usage of the shaking module in the blue stimulation group compared to orange stimulation in SNI mice. N = 10 mice (10 Blue stim videos, 9 orange stim videos), unpaired t test for each comparison, 0.16 VF *p = 0.0103, 0.6 VF **p = 0.0056, Brush *p = 0.0475, Pinprick p = 0.2956. (D) Blue light stimulation induced a conditioned place pref. 1 h post conditioning in SNI mice. N = 7 mice, Friedman's test, Dunn's multiple comparisons, pre-stim vs. real-time p = 0.1153, pre-stim vs. 1 h post **p = 0.0019, pre-stim vs. 24 h post p = 0.0518. (F) Comparison of PAWS features of blue light stimulation versus orange light stimulation in CIPN mice. ↑ = increase, ↓ = decrease, - = no change. ↓ = p < .05. See Table S5 for statistics. (G) Usage of the shaking module in the blue stimulation group compared to orange stimulation in CIPN mice. N = 9 mice (9 Blue stim videos, 9 orange stim videos), Wilcoxon test for each comparison, 0.6 VF **p = 0.0078, Brush **p = 0.0039, Pinprick p = 0.0977. (**H**) Blue light stimulation induced a conditioned place pref. 1 h and 24 h post conditioning in CIPN mice. N = 10 mice, One-way ANOVA with repeated measures, Dunnett's multiple comparisons, pre-stim vs. real-time p = 0.6468, pre-stim vs. 1 h post **p = 0.0032, pre-stim vs. 24 h post **p = 0.0013.

Tamoxifen treatment: Tamoxifen was dissolved in ethanol (20 mg/mL), mixed with an equal volume of sunflower seed oil (Sigma), vortexed for 5–10 min and centrifuged under vacuum for 20–30 min to remove the ethanol. The solution was kept at −80°C and delivered via oral gavage to pregnant females for embryonic or postnatal treatment. For all analyses, the morning after coitus was designated as E0.5 and the day of birth as P0.

Immunohistochemistry: Male and female P30-P37 mice were anesthetized with isoflurane and perfused transcardially (using an in-house gravity driven-perfusion system) with heparinized-saline (~30 s) followed by 15 min of 4% paraformaldehyde (PFA) in PBS at room temperature (RT). Brains were dissected and post-fixed in 4% PFA at 4°C for 2–24 h. Sections were collected using a vibrating microtome (Leica VT1200S) and processed for immunohistochemistry (IHC) as described previously.[166] When required, a small incision was made to the ventral brainstem to denote the side contralateral to the SNI or sham surgery. Transverse sections (50 μm) were taken of the caudal medulla containing the DCN. Free floating sections were rinsed in 50% ethanol (30 min) to increase antibody penetration, followed by three washes in a high salt PBS buffer (HS-PBS), each lasting 10 min. The tissue was then incubated in a cocktail of primary antibodies made in HS-PBS containing 0.3% Triton X-100 (HS-PBSt) for 48 at 4°C. Next, tissue was washed 3 times (10 min each) with HS-PBSt, then incubated in a secondary antibody solution made in HS-PBSt for 24 h at 4°C. Immunostained tissue was mounted on positively charged glass slides (41351253, Worldwide Medical Products) and coverslipped (48393–195, VWR) with Fluoromount-G mounting medium (100241–874, VWR).

Fluorescence *in situ* hybridization (FISH; RNAscope): Mice were anesthetized with isoflurane and perfused transcardially as described above. Medullas containing the DCN were dissected and post-fixed in 4% PFA at 4°C for 2–24 h. Samples were cryosectioned at 20 μm and processed using the RNAscope Multiplex Fluorescent v2 Assay (Advanced Cell Diagnostics, 323110). Tissue was placed in 1xPB for 5 min at room temperature then dehydrated through successive EtOH steps (50%, 70%, 100%, 100% – 5 min) and then dried at room temperature. Tissue was then treated with hydrogen peroxide for 10 min at RT, washed in water, treated with target retrieval reagents (322000) in a steamer for 5 min, and then treated with 100% EtOH for 3 min at RT. Tissue was then treated with protease III (322337) for 8 min at 40°C before being rinsed with water. Probes for Slc32a1/vGAT (Mm-Slc32a1, 319191), Slc6a5/vGlyT2 (Mm-Slc6a5, 409741), and Slc17a6/vGluT2 (Mm-Slc17a6, 456751) were hybridized for 2 h at 40°C in a humidified oven, rinsed in wash buffer, and then stored overnight in 5x saline sodium citrate. After rinsing with wash buffer, a series of incubations was performed to amplify and develop hybridized probe signals. Briefly, AMP1 (323101), AMP2 (323102), and AMP3 (323103) were successively applied for 30 min, 30 min, and 15 min at 40°C in a humidified oven, respectively, with a buffer wash in-between. For each channel, HRPC1 (323104) and/or HRPC2 (323105) and/or HRPC3 (323106) were applied for 15 min at 40°C in a humidified oven followed by a buffer wash, then treated using TSA Plus Fluorophores (PerkinElmer; NEL741001KT, NEL744001KT, and NEL745001KT), followed by 15 min of HRP blocker (323107) at 40°C in a humidified oven. Slides were then mounted with Fluoromount-G mounting medium (100241–874, VWR) with DAPI.

Image acquisition and analysis: Images were captured with a Zeiss LSM 800 confocal or a Zeiss axiovert 200M fluorescence microscope. Images for cell counts were taken with 10x or 20× air objectives, and images of synaptic contacts were taken using a 40× oil objective. ImageJ (cell count plug-in) was used for colocalization analysis of cell bodies. Imaris (spot detection plug-in) was used for synaptic analysis, quantification of synaptic terminals, and generation of contour density plots.

c-Fos induction: Mice received either an SNI surgery to induce neuropathic pain, or a sham surgery as a control. 14 days later, mice were anesthetized (5% induction, 1% maintenance) in a supine position with the plantar surface of their hindpaw exposed, and were allowed to rest for 15 min. A paintbrush (Artlicious Paint Brushes) was applied heel-to-toe with the following paradigm: 10 brushes within 10 s, every 30 s, for 30 min. 1 h later, mice were perfused and processed for immunohistochemistry. Transverse DCN sections (~50 μm) were taken and stained with rabbit anti-cFos (Synaptic Systems, 226003), mouse anti-NeuN (Millipore MAB377), and guinea pig anti-vGluT1 (Millipore AB5905). 20x images of the Gr were acquired using the Zeiss LSM 800 confocal microscope, with vGlut1 immunostaining used to identify the Gr boundaries. 4 images were analyzed per condition. c-Fos+ cells were counted, normalized to total NeuN+ cells per image.

CTb injections

Hindpaw: Mice were anesthetized (5% induction, 2–3% maintenance). Injections of 1% unconjugated CTb (~7μL across four sites) were injected into the ventral paw of C57BL/6 wild type mice to label paw sensory input. Animals were perfused 5 days after CTb injection and tissue was processed for IHC as described above. Free floating sections were immunostained with goat-CTb (list-labs). 5x images of CTb-labeled afferent inputs were taken at the Zeiss LSM 800 confocal microscope and ImageJ was used for synaptic analysis.

Stereotaxic injections

Ventral posterolateral thalamus (VPL): Mice were anesthetized with isoflurane (5% induction, 1.5–2% maintenance) and placed onto a stereotaxic frame (Stoelting) that had a feedback controlled heating blanket maintained at 36°C (FHC) on the base. The scalp was cleaned with Betadine (Purdue Products) followed by 70% ethanol (Fisher) three times. Bupivacaine (0.03 mg/kg) was injected subcutaneously into the scalp, and Meloxicam (5 mg/kg) was injected subcutaneously into the flank. A midline incision was made and the skull was exposed. The skull was leveled in the dorsoventral plane by ensuring equal bregma and lambda coordinates. Craniotomy and Injections were made following coordinates with respect to bregma: anteroposterior (AP) = −1.5 mm, mediolateral (ML) = +1.8 mm, dorsoventral (DV) = −3.5 mm. For retrograde labeling of VPL-PNS for electrophysiology and anatomical experiments, 420 nL of either pENN.AAV.CB7.CI.eGFP.WPRE.rBG (AAV9) or pENN.AAV.CB7.CI.mCherry.WPRE.RBG (AAV9) was injected into the contralateral thalamus. For retrograde targeting of VPL-PNs for chemogenetic manipulation, 420 nL of pENN.AAV.hSyn.Cre.WPRE.hGH (AAVrg) was injected into the contralateral thalamus. For all VPL injections, the micropipette was lowered down to the target depth and allowed to sit for 8 min. Virus was pressure injected over 10 min. 210 nL of the virus was injected at DV = −3.5 mm, then the micropipette was raised to DV = −3.3 mm, where the

remaining 210 nL of the virus was injected. This was followed by a 8 min period of rest to allow for diffusion of the virus into the surrounding tissue. The micropipette was then slowly raised out of the tissue. Following injections, the overlying muscle and the skin incision was sutured, and Ethiqa XR (3.25 mg/kg) was injected subcutaneously into the flank. Mice were allowed to recover from anesthesia on a heating pad, and were returned to their home cages. 2–4 weeks following the injection, mice were either perfused, and their tissue was processed for immunohistochemistry, or they were utilized for electrophysiological or behavioral experiments.

Cortex (M1, S1-Forelimb, S1-Hindlimb): Following the procedures described above, a craniotomy and injection were made at the following coordinates with respect to bregma: For M1: AP = +1.0 mm, ML = +1.7 mm, DV = −1.0 mm. For S1-forelimb (S1-FL): AP = 0 mm, ML = +2.0 mm, DV = −1.0 mm. For S1-hindlimb (S1-HL): AP = −0.5 mm, ML = +1.4, DV = −1.0 mm. For each target, 60–100 nL of AAV-phSyn1(S)-FLEX-tdTomato-T2A-SypEGFP-WPRE (Addgene, 51509) was injected at the designated coordinates. Virus was pressure injected over 10 min, and was allowed to rest for 8 min to allow for diffusion of the virus into the surrounding tissue.

Gracile nucleus (Gr): Following the procedures described above, the skin and underlying muscle surrounding the base of the skull was removed. For greater consistency of Gr injections, AP and ML coordinates were taken with respect to the caudal base of the skull, while DV coordinates were taken with respect to the cerebellar surface. A craniotomy was made at the following coordinates relative to the midline at the caudal base of the skull: AP = +0.3 mm, ML = −0.15 mm, revealing the caudal surface of the cerebellum. The micropipette was lowered to the following coordinates: AP = +0.3 mm, ML = −0.15 mm, DV = −2.00 mm and allowed to rest for 5 min. Injections of 25 nL each were made at four DV coordinates: DV = −2.00 mm, −1.95 mm, −1.90 mm, −1.85 mm, with the micropipette slowly being raised dorsally over the course of injection. Virus was pressure injected over 6 min, and allowed to rest for 8 min to allow for diffusion of the virus into the surrounding tissue. For targeting of retrogradely-labeled VPL-PNs for chemogenetics, 100 nL of pAAV1-hSyn-DIO-hM4D(Gi)-mCherry (AAV1) was injected into the ipsilateral Gr, alongside injection of 420 nL of pENN.AAV.hSyn. Cre.WPRE.hGH (AAVrg) into the contralateral VPL (described above). For chemogenetic targeting of local Gr inhibitory neurons, 100nL of pAAV1-hSyn-DIO-hM4D(Gi)-mCherry was injected into the Gr of *Vgat*$^{IRES\text{-}Cre}$ mice. As a control for chemogenetic experiments, 100 nL of pAAV-hSyn-DIO-EGFP (AAV1) was injected into the Gr of *Vgat*$^{IRES\text{-}Cre}$ mice. To visualize Gr inhibitory neurons receiving Aβ RA-LTMR input, 100 nL of pAAV-hSyn-EGFP (AAV1) was injected into the Gr of *Split*^{Cre};Ai34 mice.

Optic probe implantation

Gracile nucleus (Gr): The skull was positioned at a 20° decline to gain better optical access to the brainstem. The skin and underlying muscle surrounding the entire skull was removed. Connective tissue was removed from the skull by gentle scraping and a blue light curable bonding agent (iBond, Heraeus Kulzer) was applied to the skull to provide a better surface for dental composite to bind to. A dental drill was used to remove the caudal occipital bone,

revealing the caudal cerebellum. To gain optical access to the DCN, a needle was used to puncture the dura surrounding the cerebellum. A small portion of the caudal base of the cerebellum was aspirated to reveal the Gr. An optic cannula (ThorLabs, CFML52U-20, 4 mm length, Ø200 μm Core, 0.50 NA) was lowered to the following coordinates with respect to the obex: AP = 0 mm, ML = −0.4 mm, DV = +0.5 mm. Surrounding muscle was sutured around the cannula, and tissue glue was used to secure the optic cannula in place. Dental composite (Tetric Evoflow, Ivoclar Vivadent) was then applied to the optic cannula as well as the skull surface. Skin was sutured around the dental composite and stabilized with tissue glue. This procedure was done in *Vgat*$^{RES\text{-}Cre}$;Ai32 mice.

Spared nerve injury (SNI): To study the function of the DCN in mediating allodynia and hyperalgesia, we utilized the spared nerve injury (SNI) procedure to induce chronic neuropathic pain.[167] Mice were anesthetized and the hair surrounding the hindlimb was shaved. An incision was made on the right left below the knee, and another incision was made in the muscle to reveal the sciatic nerve. A ligature using silk suture (Braintree Scientific, SUT-S 103) was made around the peroneal and tibial nerve branches, leaving the sural nerve intact. A 2 cm portion of the peroneal/tibial nerve was cut and removed. Special care was taken to ensure that the sural nerve was not damaged during the procedure. Surrounding musculature was sutured around the nerve, and then the wound was secured using surgical wound clips (Kent Scientific, INS750344–2). Tactile hypersensitivity was determined using von Frey testing, and animals exhibiting any paralysis or desensitization were excluded from experiments.

Chemotherapy induced peripheral neuropathy (CIPN): Pharmaceutical Secondary standard Paclitaxel was dissolved in a mixture of 16% ethanol, 16% Kolliphor EL, and 68% saline. Mice received intraperitoneal injections of paclitaxel (2 mg/kg) every other day for a total of four injections (1 cycle), resulting in a cumulative dosage of 8 mg/kg.[116] Mice were tested between 7 and 21 days following the first injection, where tactile hypersensitivity has been previously described.[116]

Electrophysiology: Recordings were made from male (n = 23) and female (n = 20) mice (10.7 ± 0.4 wks). Mice used for electrophysiology were all tested for tactile hypersensitivity prior to sacrifice 11–28 days post injury (sham 15.9 ± 0.9 days and SNI 15.1 ± 0.8 days); Sham = 13 male and 10 female mice, SNI = 10 male and 10 female mice. Mice were anesthetized with ketamine (100 mg/kg i.p), decapitated, and the lumbar enlargement of the spinal cord rapidly removed in ice-cold sucrose substituted artificial cerebrospinal fluid (sACSF) containing (in mM): 250 sucrose, 25 NaHCO3, 10 glucose, 2.5 KCl, 1 NaH2PO4, 6 MgCl2, and 1 CaCl2. Sagittal or transverse slices (200μm thick) were prepared using a vibrating microtome (Leica VT1200S). Slices were incubated for at least 1 h at 22°C–24°C in an interface chamber holding oxygenated ACSF containing (in mM): 118 NaCl, 25 NaHCO3, 10 glucose, 2.5 KCl, 1 NaH2PO4, 1 MgCl2, and 2.5 CaCl2.

Following incubation, slices were transferred to a recording chamber and continually superfused with ACSF bubbled with Carbogen (95% O2 and 5% CO2) to achieve a pH of 7.3–7.4. All recordings were made at room temperature (22°C–24°C) and neurons visualized using a Zeiss Axiocam 506 color camera. Patch pipettes (3–7 MΩ) were filled with a

potassium gluconate-based internal solution containing (in mM): 135 C6H11KO7, 8 NaCl, 10 HEPES, 2 Mg2ATP, 0.3 Na3GTP, and 0.1 EGTA, (pH 7.3, adjusted with KOH, and 300 mOsm) to examine AP discharge and excitatory synaptic transmission. Recordings were acquired in cell-attached (holding current = 0mV), voltage-clamp (holding potential −70mV), or current-clamp (maintained at −60mV) configuration. The incidence of oIPSCs was also assessed using the potassium gluconate-based internal solution by holding the cell at a more depolarized potential in voltage clamp (−20 mV) to reveal hyperpolarizing potentials. A cesium chloride-based internal solution containing (in mM): 130 CsCl, 10 HEPES, 10 EGTA, 1 MgCl2, 2 Na-ATP, 2 Na-GTP, and 5 QX-314 bromide (pH 7.3, adjusted with CsOH, and 280 mOsm) was used to record inhibitory synaptic transmission in all other occasions. All recordings of sIPSCs and oIPSCs were performed in the presence of CNQX (10μM). No liquid junction potential correction was made, although this value was calculated at 14.7 mV (22°C). Slices were illuminated using an X-CITE 120LED Boost High-Power LED Illumination System that allowed visualization of mCherry (VPL-PNs, GAD2+ inhibitory neurons) with TRITC filters, and visualization of GFP fluorescence (VPL-PNs) and ChR2 photostimulation using FITC filter set.

AP discharge patterns were assessed in the current clamp from a membrane potential of −60 mV by delivering a series of depolarizing current steps (1 s duration, 20 pA increments, 0.1 Hz), with rheobase defined as the first current step that induced AP discharge. Spontaneous action potential discharge was assessed using cell-attached voltage-clamp recordings, with minimal holding current (<20 pA).

For optogenetic circuit mapping, photostimulation intensity was suprathreshold (24 mW), duration 1 ms (controlled by transistor-transistor logic pulses), 0.1 Hz. This ensured generation of action potential discharge in presynaptic populations and allowed confident assessment of postsynaptic currents in recorded neurons. When examining paired pulse ratio, an interval of 200 ms was chosen for oEPSCs and 1 s for oIPSCs.

All data were amplified using a MultiClamp 700B amplifier, digitized online (sampled at 20 kHz, filtered at 5 kHz) using an Axon Digidata 1550B, acquired and stored using Clampex software. After obtaining the whole-cell recording configuration, series resistance, input resistance, and membrane capacitance were calculated (averaged response to −5mV step, 20 trials, holding potential −70mV). A series resistance of <30 MΩ was set as a requirement for inclusion in data analysis. This resulted in the exclusion of one VPL-PN recording from a sham mouse, four inhibitory neuron recordings from sham mice, and one inhibitory neuron recording from an SNI mouse.

Electrophysiology analysis: All data were analyzed offline using AxoGraph X software.

APs were captured using a derivative threshold with AP threshold defined as the inflection point during spike initiation (dV/dt ≥ 15 V/s). AP latency was measured as the time from depolarization onset to AP threshold, AP amplitude was measured as the difference between peak amplitude and threshold, AP rise time (10–90% of AP peak), AP decay time (90–10% of AP peak), AP half-width (50% of AP peak), AHP amplitude as the difference between

AP threshold and AHP peak, and AHP half-width (50% of AHP peak). For measures of AP adaptation we compared characteristics of the first and last AP at 100 pA depolarizing current injection (when most neurons exhibit tonic firing across the entire depolarizing current step).

Optogenetically-evoked excitatory postsynaptic currents (oEPSCs) and inhibitory postsynaptic currents (oIPSCs) were measured from baseline, just before photostimulation. The peak amplitude of responses was calculated from the average of 10 successive trials. Several parameters were considered for determining whether a photostimulation-evoked synaptic input was monosynaptic or polysynaptic. The latency of oPSCs was measured as the time from photostimulation to the onset of the evoked current. The "jitter" in latency was measured as the standard deviation in latency of 10 successive trials. Importantly, the latency of monosynaptic inputs was shorter, there was minimal jitter in the onset of responses between trials, and reliability (percentage of photostimulation trials to evoke a response) was higher than those deemed polysynaptic inputs. Paired pulse ratio was determined by dividing the peak amplitude of the second pulse response by the peak amplitude of the first pulse response. Total oEPSC charge (pA.s) was measured from the time of photostimulation to the time current returned to baseline. When examining optogenetically evoked APs: The number of evoked APs was calculated as the number of APs within the first 20 ms following photostimulation; The latency and jitter of evoked APs was calculated using the first evoked AP following photostimulation; oAP reliability was calculated as the percentage of trials in which optogenetic photostimulation evoked an AP.

sEPSCs and sIPSCs were detected using a sliding template method (a semi-automated procedure in the Axograph package). Frequency was determined from at least 30s of recording at a membrane potential of −70 mV. Peak amplitude, rise time (10–90% of peak) were measured from captured events, and decay time constant (fitted over 10–90% of the decay phase) was measured from the averaged sEPSC/sIPSC for each neuron. When measuring the contributions of different neurotransmitters to sIPSC frequency, sIPSC and oIPSC amplitude, and sIPSC decay all drug responses were normalized to control conditions.

In-vivo recordings

Animal preparation and electrode implantation: C57BL/6J mice (Jax #000664) were given SNI (described above) and sent to the Salk Institute. Mice were then anesthetized with isoflurane and placed in a stereotaxic frame (Kopf Instruments) in a flat skull position. The skin and overlying fascia were incised and retracted, and the skull was cleaned with cotton swabs and dried. A small burr hole was drilled above the cerebellar vermis and a 127 μm silver wire (A-M Systems) was lowered ~1 mm below the surface of the brain and cemented in place to serve as the reference electrode for differential recordings. Next, a headplate was affixed to the skull immediately above bregma with epoxy (Tetric EvoFlow, Ivoclar Vivadent). Mice were then placed in the stereotaxic frame equipped with custom-made ear bars to allow the head to be dorsiflexed 30° from horizontal. From this position, an incision was made at the back of the head and the skin and overlying muscles were retracted to expose the obex. The most caudal portion of the occipital bone was removed to

permit access to more rostral aspects of the Gr. Finally, the dura was pierced with a 30½ gauge syringe and retracted to facilitate electrode penetration. The animal was then taken off isoflurane and administered a cocktail containing 1.2 mg/kg urethane and 20 mg/kg xylazine,[168] and transferred to a separate recording rig. The headplate was clamped in place the head was again dorsiflexed ~30° from horizontal to enable clear access to the obex and the dorsal column nuclei. The surface of the brainstem was kept moist with a layer of sterile saline or paraffin oil. Throughout recordings, animals were kept on a DC-powered heating pad to maintain stable body temperature, and supplemental doses of urethane/xylazine were given to maintain animals in an areflexic state, assessed by foot pinch.

Tactile stimuli: For all experiments, the hindlimbs were positioned on rolled gauze pads such that the glabrous footpads were oriented upwards allowing easy access for applying tactile stimuli. Tactile stimuli were applied with 2 small paintbrushes that were oriented 180° from one another and rotated across the surface of the footpad by means of a stepper motor (28BYJ-48m, MikroElektronika) controlled by a microcontroller board (Arduino UNO, Arduino). The board was triggered by a TTL pulse from a Cerebus neural signal processor (Blackrock Microsystems) and was programmed to rotate the brush-wheel at a rate of 60° per sec. There was a 7 s interval between each complete revolution (1 revolution = 2 tactile stimuli). The duration of each individual brush stimulus was ~0.7 s and the duration of a full revolution was 6 s. The entire stepper motor/brush assembly was attached to a 3-axis micromanipulator (M3301; WPI) that enabled the tactile stimuli to be applied precisely to the footpad. For each recording site within the Gr, responses to a total of 20 tactile stimuli were assessed (10 revolutions x 2 brushstrokes/rev). Stimuli were randomly alternated between the right and left footpad throughout the recording session.

Extracellular recordings: Extracellular recordings were made using carbon fiber electrodes (~0.8 MOhm, Carbostar-1, Kation Scientific) mounted to a stereotaxic manipulator (Kopf Instruments) and connected to a Cereplex M headstage (Blackrock Microsystems), which interfaced with the Cerebus neural signal processor. Signals were sampled at 30 kHz and band-pass filtered between 250 and 5000 Hz. Hindlimb responsive neurons were found within the main body of the Gr (measured relative to obex; A/p = −0.25 à +0.2 mm; M/L = 0.0 à ± 0.3mm; D/V = −0.05 à −0.20mm from the surface of the brainstem). The electrode was slowly lowered as tactile inputs were applied to the footpad and responses were monitored on an oscilloscope and through audio feedback. Robust tactile responses were typically found between 50 and 200 μm below the surface of the brainstem. All data were collected within a 4–6 h recording session and mice were perfused for histological analysis immediately following the experiment. *In vivo* electrophysiology data consisted of continuous raw data, spiking events (defined as crossing a threshold set well above noise), and analog signals marking motor outputs. Cerebus Central Suite (Blackrock Microsystems) was used to set event thresholds, and NeuroExplorer (Plexon) was used to export recording files to Excel or MATLAB (MathWorks) for further analysis. To quantify tactile evoked responses to brushstrokes applied to the hindlimbs, peri-event raster plots were generated and thresholded spikes were binned into 100 msec intervals, beginning at the initiation of motor revolution, and continuing for 6 s, encompassing the delivery of 2 brushstroke stimuli. To separate tactile evoked responses from inter-stimulus interval (ISI) spiking, each 6 s

revolution was separated into 2 individual 3.0 s intervals corresponding to a half revolution of the stepper motor. Thus, a single tactile stimulus always occurred at some point within each 3.0 s interval. Within each 3.0 s interval, we defined the window of tactile stimulation as a 0.7 s window centered on bins where the spike frequency rose to at least 200% above baseline activity, which was usually quite low. Background spiking activity was also computed for each recording site by summing the total number of spikes within a 4 s window centered in the 7 s interval between wheel revolutions. The process of computing tactile-evoked activity and background activity was repeated for each recording site. The number of spikes generated at each recording site across all 20 tactile events (10 revolutions x 2 stimuli) were then combined. The evoked and background activity were then summed across all units (both ipsilateral and contralateral to the lesioned sciatic nerve) for each mouse and paired t-tests were used to compare evoked and background activity between ipsilateral and contralateral Gr.

Behavioral testing: 7–14 weeks old male and female mice from a Bl6 (Jax#000664), CD1 (Charles River Strain#22), or mixed background were used for behavior testing.The experimenter was blind to the genotype of the animals. For all behavior assays, at least 7 days prior testing mice were transferred to the holding area adjacent to the behavior rooms. On the day of training/testing, mice were transferred to the behavior room for a 30-min habituation.

Behavior test #1: VonFrey: Von frey testing was used to assay tactile sensitivity across various stimulation strengths.[67] The testing protocol was adapted from Murthy et al., 2018.[169] 11 different von Frey filaments, ranging from .008g to 4g, were applied to the plantar hindpaw 4 times each. Withdrawal responses were recorded out of 4 total stimulations. Responses to the lowest force were recorded first before moving on to the next highest force.

Behavior test #2: Brush: Dynamic brush testing was used to assay tactile sensitivity at baseline as well as dynamic allodynia during neuropathic pain.[170] A paintbrush (Artlicious Paint Brushes) was applied to the glabrous hindpaw from heel to toe 9 times, and responses were scored from 0 to 3: 0 = no response, 1 = withdrawal, 2 = guarding, 3 = licking/tending. Responses were analyzed as the sum of all scores divided by 9 total stimulations, with a 5 min break after every 3 trials.

Behavior test #3: Pinprick: Pinprick testing was used to assess noxious mechanical sensitivity at baseline and mechanical hyperalgesia during neuropathic pain.[67] An insect pin (Austerlitz Premium Insect Entomology Dissection Pins, Size 1) was slowly raised until it made contact with the glabrous hindpaw. The number of withdrawal responses to pinprick were recorded over 10 simulations, with a 5 min break in the middle.

Behavior test #4: Hargreaves: Hargreaves testing was used to assess thermal sensitivity at baseline and thermal hyperalgesia during neuropathic pain.[171] Animals were enclosed over a glass plate, allowing for optical access to the hindpaw. A radiant heat source (IITC) was positioned underneath the animal, and aimed at the glabrous surface of the hindpaw. Intensity of the heat source was calibrated as to produce a withdrawal latency of ~10–15 s

in naive animals, as to allow for a window to capture both hypo and hyperalgesia, with a cutoff time of 20 s to avoid long term skin damage.[67] Latency to withdrawal (seconds) to the radiant heat stimulus was recorded, and averaged over 3 trials, with at least 5 min of rest between trials.

Behavior test #5: Conditioned place preference/aversion (CPP/CPA): To assess general preference/avoidance behavior of behavioral manipulations in the absence of any evoked sensory responses, we utilized the two-chamber CPP/CPA assay.[172] For chemogenetic experiments, mice were allowed to freely explore both chambers on Day 1 for 10 min to establish initial preference. On Days 2–5, chambers were closed off, and mice were conditioned to saline on one side in the morning, and CNO on the other side in the evening, for 30 min each. To remove bias of time of day, conditioning to saline/CNO was swapped between morning and evening sessions every day. On Day 6, mice were once again allowed to freely explore both chambers to establish CPP/CPA. For optogenetic experiments, mice were allowed to freely explore the chambers in the morning on Day 1 for 10 min to establish initial preference. Following this initial session, mice were optically stimulated with continuous light on the side they preferred less, using a 2 s on, 2 s off paradigm. This first session was used to establish "real-time' placed preference. This was repeated in the evening on Day 1, as well as a morning and evening session on Day 2, for a total of 4 sessions. On Days 2 and 3, mice were allowed to freely explore the chambers without any optical stimulation to determine if conditioning was retained 1 h and 24 h after the final stimulating session.

Behavior test #5: Data generation for PAWS and B-SOiD: To generate data for PAWS analysis, mice were placed in clear plexiglass chambers positioned perpendicular to a camera (FASTCAM Mini AX100, ZEISS Milvus 100mm f/2M ZF.2 lens). Barriers were placed so that animals were not able to see each other. Mice were habituated for a minimum of 3 days prior to the testing date, and habituated in the chambers for 30 min prior to testing. A maximum of two different simulations were applied per day, a minimum of 6 h apart, to limit the effects of prior stimulations on future responses. Stimulations were also delivered in order from most innocuous to most noxious (0.16 VF → 0.6 VF → brush → pinprick). Mouse behaviors were recorded at 4000 FPS, and video durations were approximately 1.25 s. The camera was placed at a 10° angle facing downwards toward the animal, approximately 3 feet away from the plexiglass chambers. Infrared lights were used to illuminate the scene.

Videos were processed by DeepLabCut[97] to predict the location of the toe, metatarsophalangeal joint (MTP), heel, and reference positions from the plexiglass box (top left corner and bottom left corner). We utilized DeepLabCut for markerless pose estimation of body parts. The software provides an open-source toolbox that facilitates the extraction of frames, annotation of body parts, training of a deep neural network, and subsequent tracking of body parts using the trained model. The network is finetuned on frames extracted from videos and the accompanying labels marking the locations of the body parts, training the architecture end to end. We extracted 20 frames from a random sample of our collected videos through the DeepLabCut toolbox and annotated the toe, MTP, and the top and the

bottom corners on the left side of the box containing the mouse. We observed the greatest confidence of tracking for the MTP, which we then used for all analyses. The annotated frames were then used to train the pose estimation network and track the body parts on unlabeled frames through the full length of our collected videos. Labeled data was then run through the PAWS[91] software for feature extraction.

Analysis of PAWS data: Paw withdrawal tracking data was analyzed using the Pain Assessment at Withdrawal Speeds (PAWS) software.[91] Coordinates for the metatarsophalangeal joint (MTP) were used to extract features of the paw withdrawal, including max height, distance traveled, max velocity, # of shakes, and guarding duration. Data points under 80% tracking confidence were excluded from the analysis, and a rolling average filter was applied for data smoothing.

B-SOiD analysis: To quantify behavior following foot stimulation, pose estimation data output by DeepLabCut was imported into the unsupervised behavioral discovery algorithm, B-SOiD, following previously described methods.[99] Briefly, data was first converted from pixel units to millimeter units, and downsampled to 1/14th of the original frame rate. Additionally, two static reference points for each video were computed: a) the initial position of the toe, and b) the toe position at the maximum elevation reached post-stimulation. The coordinates of the toe, MTP, and two reference points were selected for feature extraction, non-linear embedding into UMAP space. HDBSCAN (parameters: min_samples = 10; minimum cluster size range = 0.1%–1.0%) was used to identify nine behavioral clusters. Cluster assignments were used to train a random forest classifier to predict behavioral clusters from extracted features, and this model was run on the full dataset. Behavioral clusters were given post-hoc ethological labels by expert raters. Clusters representing less than 1% of all frames were excluded from further analysis. The normalized number of frames labeled by each cluster starting from the initial withdrawal response was computed and plotted using matplotlib.

QUANTIFICATION AND STATISTICAL ANALYSIS

All data are reported as mean values ± the standard error of the mean (SEM), unless otherwise stated. Statistical analysis was performed in GraphPad Prism (USA) or MATLAB. All data was tested for normality using the Shapiro-Wilk test. For all tests *$p < 0.05$, **$p < 0.05$, ***$p < 0.005$, and ****$p \leq 0.0005$. The means of different data distributions were compared using One-way ANOVA, Tukey's multiple comparisons (Figures 1F and 1G), Unpaired t test (Figures 1K, 1L, 2H, 5Q, 6L, 7C), Mann-Whitney test (Figures 2D, 2G, 2K, 2L, 2M, 2N, 3C, 5B, 5I, 5J, 5K, 5L, and 5O), Mixed-effects model with Geisser-Greenhouse correction and Sidak's multiple comparisons test (Figure 2F), One-Way ANOVA with Dunnett's multiple comparisons test (Figures 3L, 3R, and 7H), Kruskal-Wallis with Dunn's multiple comparisons test (Figures 3O, 3P, and 4K), two-way ANOVA with Sidaks multiple comparisons test (Figures 4C and 6I), Wilcoxon test (Figures 4D, 4H, 6D, 6H, 6J, and 7G), two-way ANOVA with Tukey's multiple comparisons test (Figures 4G, 6C, and 6G), Paired t test (Figures 4L, 5D, and 5E), and Friedman's with Dunn's multiple comparisons test (Figure 7D). Statistics details for supplemental figures can be found in supplemental figure legends.

Supplementary Material

Refer to Web version on PubMed Central for supplementary material.

ACKNOWLEDGMENTS

We are grateful to Dr. Sliman Bensmaia for providing macaque brain stem tissue and Yurdiana Hernandez for assistance with genotyping. Financial support was provided by the NIH/National Institute of Neurological Disorders and Stroke (NINDS) grant nos. K99NS133476 (M.A.G.), K01NS116224 (V.E.A.), R01NS119268 (V.E.A.), R01NS124799 (V.E.A.), and R01NS124799 (E.A.); the New Jersey Commission on Spinal Cord Research (M.A.G. and V.E.A.); the Pew Charitable Trust (V.E.A.); the Rita Allen Foundation (V.E.A.); the NIH grant nos. DP2NS105555 (E.A.) and RF1NS128898 (E.A.); and the LIFE Foundation (E.A.).

REFERENCES

1. Lolignier S, Eijkelkamp N, and Wood JN (2015). Mechanical allodynia. Pflugers Arch 467, 133–139. [PubMed: 24846747]
2. Jensen TS, and Finnerup NB (2014). Allodynia and hyperalgesia in neuropathic pain: clinical manifestations and mechanisms. Lancet Neurol 13, 924–935. [PubMed: 25142459]
3. Kuner R (2010). Central mechanisms of pathological pain. Nat. Med 16, 1258–1266. [PubMed: 20948531]
4. Gold MS, and Gebhart GF (2010). Nociceptor sensitization in pain pathogenesis. Nat. Med 16, 1248–1257. [PubMed: 20948530]
5. Gangadharan V, Zheng H, Taberner FJ, Landry J, Nees TA, Pistolic J, Agarwal N, Männich D, Benes V, Helmstaedter M, et al. (2022). Neuropathic pain caused by miswiring and abnormal end organ targeting. Nature 606, 137–145. [PubMed: 35614217]
6. Boyle KA, Gradwell MA, Yasaka T, Dickie AC, Polgár E, Ganley RP, Orr DPH, Watanabe M, Abraira VE, Kuehn ED, et al. (2019). Defining a Spinal Microcircuit that Gates Myelinated Afferent Input: Implications for Tactile Allodynia. Cell Rep 28, 526–540.e6. [PubMed: 31291586]
7. Peirs C, Williams SPG, Zhao X, Arokiaraj CM, Ferreira DW, Noh MC, Smith KM, Halder P, Corrigan KA, Gedeon JY, et al. (2021). Mechanical allodynia circuitry in the dorsal horn is defined by the nature of the injury. Neuron 109, 73–90.e7. [PubMed: 33181066]
8. Sun L, Liu R, Guo F, Wen MQ, Ma XL, Li KY, Sun H, Xu CL, Li YY, Wu MY, et al. (2020). Parabrachial nucleus circuit governs neuropathic pain-like behavior. Nat. Commun 11, 5974–6021. [PubMed: 33239627]
9. Wang Z, and Xu Z-Z (2021). The Parabrachial Nucleus as a Key Regulator of Neuropathic Pain. Neurosci. Bull 37, 1079–1081. [PubMed: 33929705]
10. Miyamoto K, Kume K, and Ohsawa M (2017). Role of microglia in mechanical allodynia in the anterior cingulate cortex. J. Pharmacol. Sci 134, 158–165. [PubMed: 28669596]
11. Mansikka H, and Pertovaara A (1997). Supraspinal influence on hindlimb withdrawal thresholds and mustard oil-induced secondary allodynia in rats. Brain Res. Bull 42, 359–365. [PubMed: 9092877]
12. Sung B, Na HS, Kim YI, Yoon YW, Han HC, Nahm SH, and Hong SK (1998). Supraspinal involvement in the production of mechanical allodynia by spinal nerve injury in rats. Neurosci. Lett 246, 117–119. [PubMed: 9627194]
13. Malan TP, Ossipov MH, Gardell LR, Ibrahim M, Bian D, Lai J, and Porreca F (2000). Extraterritorial neuropathic pain correlates with multisegmental elevation of spinal dynorphin in nerve-injured rats. Pain 86, 185–194. [PubMed: 10779675]
14. Bian D, Ossipov MH, Zhong C, Malan TP, and Porreca F (1998). Tactile allodynia, but not thermal hyperalgesia, of the hindlimbs is blocked by spinal transection in rats with nerve injury. Neurosci. Lett 241, 79–82. [PubMed: 9507925]
15. Shankarappa SA, Tsui JH, Kim KN, Reznor G, Dohlman JC, Langer R, and Kohane DS (2012). Prolonged nerve blockade delays the onset of neuropathic pain. Proc. Natl. Acad. Sci. USA 109, 17555–17560. [PubMed: 23045676]

16. Delhaye BP, Long KH, and Bensmaia SJ (2018). Neural Basis of Touch and Proprioception in Primate Cortex. Compr. Physiol 8, 1575–1602. [PubMed: 30215864]
17. Loutit AJ, Vickery RM, and Potas JR (2021). Functional organization and connectivity of the dorsal column nuclei complex reveals a sensorimotor integration and distribution hub. J. Comp. Neurol 529, 187–220. [PubMed: 32374027]
18. Sun H, Ren K, Zhong CM, Ossipov MH, Malan TP, Lai J, and Porreca F (2001). Nerve injury-induced tactile allodynia is mediated via ascending spinal dorsal column projections. Pain 90, 105–111. [PubMed: 11166976]
19. Gmel GE, Santos Escapa R, Benkohen TE, Mugan D, Parker JL, and Palmisani S (2023). Postsynaptic dorsal column pathway activation during spinal cord stimulation in patients with chronic pain. Front. Neurosci 17, 1297814. [PubMed: 38188030]
20. Schwark HD, and Ilyinsky OB (2001). Inflammatory pain reduces correlated activity in the dorsal column nuclei. Brain Res 889, 295–302. [PubMed: 11166722]
21. Kim HY, Wang J, and Gwak YS (2012). Gracile neurons contribute to the maintenance of neuropathic pain in peripheral and central neuropathic models. J. Neurotrauma 29, 2587–2592. [PubMed: 22794293]
22. Miki K, Iwata K, Tsuboi Y, Sumino R, Fukuoka T, Tachibana T, Tokunaga A, and Noguchi K (1998). Responses of dorsal column nuclei neurons in rats with experimental mononeuropathy. Pain 76, 407–415. [PubMed: 9718259]
23. Shortland P, and Molander C (1998). The time-course of abeta-evoked c-fos expression in neurons of the dorsal horn and gracile nucleus after peripheral nerve injury. Brain Res 810, 288–293. [PubMed: 9813372]
24. Persson JK, Hongpaisan J, and Molander C (1993). c-fos expression in gracilothalamic tract neurons after electrical stimulation of the injured sciatic nerve in the adult rat. Somatosens. Mot. Res 10, 475–483. [PubMed: 8310784]
25. Tsuda M (2016). Microglia in the spinal cord and neuropathic pain. J. Diabetes Investig 7, 17–26.
26. Magnussen C, Hung S-P, and Ribeiro-da-Silva A (2015). Novel expression pattern of neuropeptide Y immunoreactivity in the peripheral nervous system in a rat model of neuropathic pain. Mol. Pain 11, 31. [PubMed: 26012590]
27. Zou Y, Xu F, Tang Z, Zhong T, Cao J, Guo Q, and Huang C (2016). Distinct calcitonin gene-related peptide expression pattern in primary afferents contribute to different neuropathic symptoms following chronic constriction or crush injuries to the rat sciatic nerve. Mol. Pain 12, 1744806916681566. [PubMed: 28256957]
28. Hughes DI, Scott DT, Riddell JS, and Todd AJ (2007). Upregulation of substance P in low-threshold myelinated afferents is not required for tactile allodynia in the chronic constriction injury and spinal nerve ligation models. J. Neurosci 27, 2035–2044. [PubMed: 17314299]
29. (2010). Upregulation of the GABA transporter GAT-1 in the gracile nucleus in the spared nerve injury model of neuropathic pain. Neurosci. Lett 480, 132–137. [PubMed: 20542084]
30. Liljencrantz J, and Olausson H (2014). Tactile C fibers and their contributions to pleasant sensations and to tactile allodynia. Front. Behav. Neurosci 8, 37. [PubMed: 24639633]
31. Tashima R, Koga K, Sekine M, Kanehisa K, Kohro Y, Tominaga K, Matsushita K, Tozaki-Saitoh H, Fukazawa Y, Inoue K, et al. (2018). Optogenetic Activation of Non-Nociceptive Aβ Fibers Induces Neuropathic Pain-Like Sensory and Emotional Behaviors after Nerve Injury in Rats. eNeuro 5, ENEURO.0450–17.2018.
32. Dhandapani R, Arokiaraj CM, Taberner FJ, Pacifico P, Raja S, Nocchi L, Portulano C, Franciosa F, Maffei M, Hussain AF, et al. (2018). Control of mechanical pain hypersensitivity in mice through ligand-targeted photoablation of TrkB-positive sensory neurons. Nat. Commun 9, 1640. [PubMed: 29691410]
33. Gautam M, Yamada A, Yamada A, Wu Q, Kridsada K, Ling J, Yu H, Dong P, Ma M, Gu J, and Luo W (2023). Distinct Local and Global Functions of Aβ Low-Threshold Mechanoreceptors in Mechanical Pain Transmission. Preprint at Res. Sq 10.21203/rs.3.rs-2939309/v1.
34. Suresh AK, Greenspon CM, He Q, Rosenow JM, Miller LE, and Bensmaia SJ (2021). Sensory computations in the cuneate nucleus of macaques. Proc. Natl. Acad. Sci. USA 118, e2115772118. [PubMed: 34853173]

35. Versteeg C, Rosenow JM, Bensmaia SJ, and Miller LE (2021). Encoding of limb state by single neurons in the cuneate nucleus of awake monkeys. J. Neurophysiol 126, 693–706. [PubMed: 34010577]
36. Versteeg C, Chowdhury RH, and Miller LE (2021). Cuneate nucleus: The somatosensory gateway to the brain. Curr. Opin. Physiol 20, 206–215. [PubMed: 33869911]
37. Turecek J, Lehnert BP, and Ginty DD (2022). The encoding of touch by somatotopically aligned dorsal column subdivisions. Nature 612, 310–315. [PubMed: 36418401]
38. Marino J, Canedo A, and Aguilar J (2000). Sensorimotor cortical influences on cuneate nucleus rhythmic activity in the anesthetized cat. Neuroscience 95, 657–673. [PubMed: 10670434]
39. Andersen P, Eccles JC, Oshima T, and Schmidt RF (1964). MECHANISMS OF SYNAPTIC TRANSMISSION IN THE CUNEATE NUCLEUS. J. Neurophysiol 27, 1096–1116. [PubMed: 14223972]
40. Canedo A, Martinez L, and Mariño J (1998). Tonic and bursting activity in the cuneate nucleus of the chloralose-anesthetized cat. Neuroscience 84, 603–617. [PubMed: 9580341]
41. Dykes RW, Rasmusson DD, Sretavan D, and Rehman NB (1982). Submodality segregation and receptive-field sequences in cuneate, gracile, and external cuneate nuclei of the cat. J. Neurophysiol 47, 389–416. [PubMed: 6461730]
42. Mariño J, Martinez L, and Canedo A (1999). Sensorimotor Integration at the Dorsal Column Nuclei. News Physiol. Sci 14, 231–237. [PubMed: 11390857]
43. Conner JM, Bohannon A, Igarashi M, Taniguchi J, Baltar N, and Azim E (2021). Modulation of tactile feedback for the execution of dexterous movement. Science 374, 316–323. [PubMed: 34648327]
44. Guo D, and Hu J (2014). Spinal presynaptic inhibition in pain control. Neuroscience 283, 95–106. [PubMed: 25255936]
45. Sivilotti L, and Woolf CJ (1994). The contribution of GABAA and glycine receptors to central sensitization: disinhibition and touch-evoked allodynia in the spinal cord. J. Neurophysiol 72, 169–179. [PubMed: 7965003]
46. Roberts LA, Beyer C, and Komisaruk BR (1986). Nociceptive responses to altered GABAergic activity at the spinal cord. Life Sci 39, 1667–1674. [PubMed: 3022091]
47. Enna SJ, and McCarson KE (2006). The role of GABA in the mediation and perception of pain. Adv. Pharmacol 54, 1–27. [PubMed: 17175808]
48. Comitato A, and Bardoni R (2021). Presynaptic Inhibition of Pain and Touch in the Spinal Cord: From Receptors to Circuits. Int. J. Mol. Sci 22, 414. [PubMed: 33401784]
49. Baba H, Ji RR, Kohno T, Moore KA, Ataka T, Wakai A, Okamoto M, and Woolf CJ (2003). Removal of GABAergic inhibition facilitates polysynaptic A fiber-mediated excitatory transmission to the superficial spinal dorsal horn. Mol. Cell. Neurosci 24, 818–830. [PubMed: 14664828]
50. Lu Y, Dong H, Gao Y, Gong Y, Ren Y, Gu N, Zhou S, Xia N, Sun YY, Ji RR, and Xiong L (2013). A feed-forward spinal cord glycinergic neural circuit gates mechanical allodynia. J. Clin. Investig 123, 4050–4062. [PubMed: 23979158]
51. Wercberger R, and Basbaum AI (2019). Spinal cord projection neurons: a superficial, and also deep, analysis. Curr. Opin. Physiol 11, 109–115. [PubMed: 32864531]
52. Paixão S, Loschek L, Gaitanos L, Alcalà Morales P, Goulding M, and Klein R (2019). Identification of Spinal Neurons Contributing to the Dorsal Column Projection Mediating Fine Touch and Corrective Motor Movements. Neuron 104, 749–764.e6. [PubMed: 31586516]
53. Browne TJ, Smith KM, Gradwell MA, Iredale JA, Dayas CV, Callister RJ, Hughes DI, and Graham BA (2021). Spinoparabrachial projection neurons form distinct classes in the mouse dorsal horn. Pain 162, 1977–1994. [PubMed: 33779126]
54. Todd AJ, Puskar Z, Spike RC, Hughes C, Watt C, and Forrest L (2002). Projection neurons in lamina I of rat spinal cord with the neurokinin 1 receptor are selectively innervated by substance p-containing afferents and respond to noxious stimulation. J. Neurosci 22, 4103–4113. [PubMed: 12019329]

55. Agashkov K, Krotov V, Krasniakova M, Shevchuk D, Andrianov Y, Zabenko Y, Safronov BV, Voitenko N, and Belan P (2019). Distinct mechanisms of signal processing by lamina I spino-parabrachial neurons. Sci. Rep 9, 19231. [PubMed: 31848358]
56. Koch SC, Acton D, and Goulding M (2018). Spinal Circuits for Touch, Pain, and Itch. Annu. Rev. Physiol 80, 189–217. [PubMed: 28961064]
57. Hughes DI, and Todd AJ (2020). Central Nervous System Targets: Inhibitory Interneurons in the Spinal Cord. Neurotherapeutics 17, 874–885. [PubMed: 33029722]
58. Todd AJ (2017). Identifying functional populations among the interneurons in laminae I-III of the spinal dorsal horn. Mol. Pain 13, 1744806917693003. [PubMed: 28326935]
59. Bardoni R, Takazawa T, Tong CK, Choudhury P, Scherrer G, and Macdermott AB (2013). Pre- and postsynaptic inhibitory control in the spinal cord dorsal horn. Ann. N. Y. Acad. Sci 1279, 90–96. [PubMed: 23531006]
60. Sullivan SJ, and Sdrulla AD (2022). Excitatory and Inhibitory Neurons of the Spinal Cord Superficial Dorsal Horn Diverge in Their Somatosensory Responses and Plasticity in Vivo. J. Neurosci 42, 1958–1973. [PubMed: 35046121]
61. Abraira VE, Kuehn ED, Chirila AM, Springel MW, Toliver AA, Zimmerman AL, Orefice LL, Boyle KA, Bai L, Song BJ, et al. (2017). The Cellular and Synaptic Architecture of the Mechanosensory Dorsal Horn. Cell 168, 295–310.e19. [PubMed: 28041852]
62. Moehring F, Halder P, Seal RP, and Stucky CL (2018). Uncovering the Cells and Circuits of Touch in Normal and Pathological Settings. Neuron 100, 349–360. [PubMed: 30359601]
63. Tashima R, Koga K, Yoshikawa Y, Sekine M, Watanabe M, Tozaki-Saitoh H, Furue H, Yasaka T, and Tsuda M (2021). A subset of spinal dorsal horn interneurons crucial for gating touch-evoked pain-like behavior. Proc. Natl. Acad. Sci. USA 118, e2021220118. [PubMed: 33431693]
64. Chen S, Gao XF, Zhou Y, Liu BL, Liu XY, Zhang Y, Barry DM, Liu K, Jiao Y, Bardoni R, et al. (2020). A spinal neural circuitry for converting touch to itch sensation. Nat. Commun 11, 5074. [PubMed: 33033265]
65. Foster E, Wildner H, Tudeau L, Haueter S, Ralvenius WT, Jegen M, Johannssen H, Hösli L, Haenraets K, Ghanem A, et al. (2015). Targeted ablation, silencing, and activation establish glycinergic dorsal horn neurons as key components of a spinal gate for pain and itch. Neuron 85, 1289–1304. [PubMed: 25789756]
66. Escalante A, and Klein R (2020). Spinal Inhibitory Ptf1a-Derived Neurons Prevent Self-Generated Itch. Cell Rep 33, 108422. [PubMed: 33238109]
67. Deuis JR, Dvorakova LS, and Vetter I (2017). Methods Used to Evaluate Pain Behaviors in Rodents. Front. Mol. Neurosci 10, 284. [PubMed: 28932184]
68. Lehnert BP, Santiago C, Huey EL, Emanuel AJ, Renauld S, Africawala N, Alkislar I, Zheng Y, Bai L, Koutsioumpa C, et al. (2021). Mechanoreceptor synapses in the brainstem shape the central representation of touch. Cell 184, 5608–5621.e18. [PubMed: 34637701]
69. Niu J, Ding L, Li JJ, Kim H, Liu J, Li H, Moberly A, Badea TC, Duncan ID, Son YJ, et al. (2013). Modality-based organization of ascending somatosensory axons in the direct dorsal column pathway. J. Neurosci 33, 17691–17709. [PubMed: 24198362]
70. Giuffrida R, and Rustioni A (1992). Dorsal root ganglion neurons projecting to the dorsal column nuclei of rats. J. Comp. Neurol. 316, 206–220. [PubMed: 1374085]
71. Thompson SJ, Millecamps M, Aliaga A, Seminowicz DA, Low LA, Bedell BJ, Stone LS, Schweinhardt P, and Bushnell MC (2014). Metabolic brain activity suggestive of persistent pain in a rat model of neuropathic pain. Neuroimage 91, 344–352. [PubMed: 24462776]
72. Chen C, Sun L, Adler A, Zhou H, Zhang L, Zhang L, Deng J, Bai Y, Zhang J, Yang G, et al. (2023). Synchronized activity of sensory neurons initiates cortical synchrony in a model of neuropathic pain. Nat. Commun 14, 689. [PubMed: 36755026]
73. Chao T-HH, Chen J-H, and Yen C-T (2018). Plasticity changes in forebrain activity and functional connectivity during neuropathic pain development in rats with sciatic spared nerve injury. Mol. Brain 11, 55. [PubMed: 30285801]
74. Bray N (2017). Pain: A painful loss of inhibition. Nat. Rev. Neurosci 18, 456.
75. Ab Aziz CB, and Ahmad AH (2006). The role of the thalamus in modulating pain. Malays. J. Med. Sci 13, 11–18. [PubMed: 22589599]

76. Wang Z, Huang S, Yu X, Li L, Yang M, Liang S, Liu W, and Tao J (2020). Altered thalamic neurotransmitters metabolism and functional connectivity during the development of chronic constriction injury induced neuropathic pain. Biol. Res 53, 36. [PubMed: 32843088]
77. Chambers WW, Liu CN, and McCOUCH GP (1963). Inhibition of the dorsal column nuclei. Exp. Neurol 7, 13–23. [PubMed: 14019957]
78. Schwark HD, Tennison CF, Ilyinsky OB, and Fuchs JL (1999). Inhibitory influences on receptive field size in the dorsal column nuclei. Exp. Brain Res 126, 439–442. [PubMed: 10382628]
79. Jabbur SJ, and Banna NR (1970). Widespread cutaneous inhibition in dorsal column nuclei. J. Neurophysiol 33, 616–624. [PubMed: 4318172]
80. Andersen P, Etholm B, and Gordon G (1970). Presynaptic and postsynaptic inhibition elicited in the cat's dorsal column nuclei by mechanical stimulation of skin. J. Physiol 210, 433–455. [PubMed: 5501269]
81. Chaudhry FA, Reimer RJ, Bellocchio EE, Danbolt NC, Osen KK, Edwards RH, and Storm-Mathisen J (1998). The vesicular GABA transporter, VGAT, localizes to synaptic vesicles in sets of glycinergic as well as GABAergic neurons. J. Neurosci 18, 9733–9750. [PubMed: 9822734]
82. Berkley KJ, and Hubscher CH (1995). Are there separate central nervous system pathways for touch and pain? Nat. Med 1, 766–773. [PubMed: 7585178]
83. Nathan PW, Smith MC, and Cook AW (1986). Sensory effects in man of lesions of the posterior columns and of some other afferent pathways. Brain 109, 1003–1041. [PubMed: 3096488]
84. Vierck CJ Jr. (1978). Comparison of forelimb and hindlimb motor deficits following dorsal column section in monkeys. Brain Res 146, 279–294. [PubMed: 417758]
85. Ballermann M, McKenna J, and Whishaw IQ (2001). A grasp-related deficit in tactile discrimination following dorsal column lesion in the rat. Brain Res. Bull 54, 237–242. [PubMed: 11275414]
86. Houghton AK, Hewitt E, and Westlund KN (1999). Dorsal column lesion prevents mechanical hyperalgesia and allodynia in osteotomy model. Pain 82, 73–80. [PubMed: 10422662]
87. White JC (1950). Neurosurgical treatment of persistent pain. Lancet 2, 161–164. [PubMed: 15437909]
88. Condon LF, Yu Y, Park S, Cao F, Pauli JL, Nelson TS, and Palmiter RD (2024). Parabrachial Calca neurons drive nociplasticity. Cell Rep 43, 114057. [PubMed: 38583149]
89. Torsney C, and MacDermott AB (2006). Disinhibition opens the gate to pathological pain signaling in superficial neurokinin 1 receptor-expressing neurons in rat spinal cord. J. Neurosci 26, 1833–1843. [PubMed: 16467532]
90. Sun S, Xu Q, Guo C, Guan Y, Liu Q, and Dong X (2017). Leaky Gate Model: Intensity-Dependent Coding of Pain and Itch in the Spinal Cord. Neuron 93, 840–853.e5. [PubMed: 28231466]
91. Jones JM, Foster W, Twomey CR, Burdge J, Ahmed OM, Pereira TD, Wojick JA, Corder G, Plotkin JB, and Abdus-Saboor I (2020). A machine-vision approach for automated pain measurement at millisecond timescales. Elife 9, e57258. [PubMed: 32758355]
92. Hsu AI, and Yttri EA (2021). B-SOiD, an open-source unsupervised algorithm for identification and fast prediction of behaviors. Nat. Commun 12, 5188. [PubMed: 34465784]
93. Yaksh TL (1989). Behavioral and autonomic correlates of the tactile evoked allodynia produced by spinal glycine inhibition: effects of modulatory receptor systems and excitatory amino acid antagonists. Pain 37, 111–123. [PubMed: 2542867]
94. Choi J-H, Choi JH, Sim JH, Lee S, Ahn HS, and Choi SS (2015). Development of tactile allodynia immediately after spinal anesthesia. Pain Med 16, 1242–1244. [PubMed: 25651126]
95. La J-H, and Chung JM (2017). Peripheral afferents and spinal inhibitory system in dynamic and static mechanical allodynia. Pain 158, 2285–2289. [PubMed: 28885453]
96. Zhang Z, Hefferan MP, and Loomis CW (2001). Topical bicuculline to the rat spinal cord induces highly localized allodynia that is mediated by spinal prostaglandins. Pain 92, 351–361. [PubMed: 11376908]
97. Mathis A, Mamidanna P, Cury KM, Abe T, Murthy VN, Mathis MW, and Bethge M (2018). DeepLabCut: markerless pose estimation of user-defined body parts with deep learning. Nat. Neurosci 21, 1281–1289. [PubMed: 30127430]

98. Cichon J, Sun L, and Yang G (2018). Spared Nerve Injury Model of Neuropathic Pain in Mice. Bio. Protoc 8, e2777.

99. Bohic M, Pattison LA, Jhumka ZA, Rossi H, Thackray JK, Ricci M, Mossazghi N, Foster W, Ogundare S, Twomey CR, et al. (2023). Mapping the neuroethological signatures of pain, analgesia, and recovery in mice. Neuron 111, 2811–2830.e8. [PubMed: 37442132]

100. Borst JG, and Sakmann B (1999). Effect of changes in action potential shape on calcium currents and transmitter release in a calyx-type synapse of the rat auditory brainstem. Philos. Trans. R. Soc. Lond. B Biol. Sci 354, 347–355. [PubMed: 10212483]

101. Mendonça PRF, Tagliatti E, Langley H, Kotzadimitriou D, Zamora-Chimal CG, Timofeeva Y, and Volynski KE (2022). Asynchronous glutamate release is enhanced in low release efficacy synapses and dispersed across the active zone. Nat. Commun 13, 3497. [PubMed: 35715404]

102. Taylor BK (2009). Spinal inhibitory neurotransmission in neuropathic pain. Curr. Pain Headache Rep 13, 208–214. [PubMed: 19457281]

103. Vaysse L, Sol JC, Lazorthes Y, Courtade-Saidi M, Eaton MJ, and Jozan S (2011). GABAergic pathway in a rat model of chronic neuropathic pain: modulation after intrathecal transplantation of a human neuronal cell line. Neurosci. Res 69, 111–120. [PubMed: 20970463]

104. Jergova S, Hentall ID, Gajavelli S, Varghese MS, and Sagen J (2012). Intraspinal transplantation of GABAergic neural progenitors attenuates neuropathic pain in rats: a pharmacologic and neurophysiological evaluation. Exp. Neurol 234, 39–49. [PubMed: 22193109]

105. Bráz JM, Sharif-Naeini R, Vogt D, Kriegstein A, Alvarez-Buylla A, Rubenstein JL, and Basbaum AI (2012). Forebrain GABAergic neuron precursors integrate into adult spinal cord and reduce injury-induced neuropathic pain. Neuron 74, 663–675. [PubMed: 22632725]

106. Gwak YS, Tan HY, Nam TS, Paik KS, Hulsebosch CE, and Leem JW (2006). Activation of spinal GABA receptors attenuates chronic central neuropathic pain after spinal cord injury. J. Neurotrauma 23, 1111–1124. [PubMed: 16866624]

107. Hamilton LS, Sohl-Dickstein J, Huth AG, Carels VM, Deisseroth K, and Bao S (2013). Optogenetic activation of an inhibitory network enhances feedforward functional connectivity in auditory cortex. Neuron 80, 1066–1076. [PubMed: 24267655]

108. Moon HS, Jiang H, Vo TT, Jung WB, Vazquez AL, and Kim SG (2021). Contribution of Excitatory and Inhibitory Neuronal Activity to BOLD fMRI. Cereb. Cortex 31, 4053–4067. [PubMed: 33895810]

109. Babl SS, Rummell BP, and Sigurdsson T (2019). The Spatial Extent of Optogenetic Silencing in Transgenic Mice Expressing Channelrhodopsin in Inhibitory Interneurons. Cell Rep 29, 1381–1395.e4. [PubMed: 31665647]

110. Gu L, Uhelski ML, Anand S, Romero-Ortega M, Kim Y.t., Fuchs PN, and Mohanty SK (2015). Pain inhibition by optogenetic activation of specific anterior cingulate cortical neurons. PLoS One. 10, e0117746. [PubMed: 25714399]

111. Lin JY (2011). A user's guide to channelrhodopsin variants: features, limitations and future developments. Exp. Physiol 96, 19–25. [PubMed: 20621963]

112. Schoenenberger P, Gerosa D, and Oertner TG (2009). Temporal control of immediate early gene induction by light. PLoS One. 4, e8185. [PubMed: 19997631]

113. Ishizuka T, Kakuda M, Araki R, and Yawo H (2006). Kinetic evaluation of photosensitivity in genetically engineered neurons expressing green algae light-gated channels. Neurosci. Res 54, 85–94. [PubMed: 16298005]

114. Lin JY, Lin MZ, Steinbach P, and Tsien RY (2009). Characterization of engineered channelrhodopsin variants with improved properties and kinetics. Biophys. J 96, 1803–1814. [PubMed: 19254539]

115. Britt JP, McDevitt RA, and Bonci A (2012). Use of channelrhodopsin for activation of CNS neurons. Curr. Protoc. Neurosci 58, 2–16.

116. Toma W, Kyte SL, Bagdas D, Alkhlaif Y, Alsharari SD, Lichtman AH, Chen ZJ, Del Fabbro E, Bigbee JW, Gewirtz DA, and Damaj MI (2017). Effects of paclitaxel on the development of neuropathy and affective behaviors in the mouse. Neuropharmacology 117, 305–315. [PubMed: 28237807]

117. Beijers AJM, Jongen JLM, and Vreugdenhil G (2012). Chemotherapy-induced neurotoxicity: the value of neuroprotective strategies. Neth. J. Med 70, 18–25. [PubMed: 22271810]
118. Pennypacker SD, Fonseca MM, Morgan JW, Dougherty PM, Cubillos-Ruiz JR, Strowd RE, and Romero-Sandoval EA (2022). Methods and protocols for chemotherapy-induced peripheral neuropathy (CIPN) mouse models using paclitaxel. Methods Cell Biol 168, 277–298. [PubMed: 35366987]
119. Sufka KJ (1994). Conditioned place preference paradigm: a novel approach for analgesic drug assessment against chronic pain. Pain 58, 355–366. [PubMed: 7838585]
120. Lundberg A (1979). Multisensory Control of Spinal Reflex Pathways. In Progress in Brain Research, 50, Granit R and Pompeiano O, eds. (Elsevier), pp. 11–28. [PubMed: 121776]
121. Morgan MM (1998). Direct comparison of heat-evoked activity of nociceptive neurons in the dorsal horn with the hindpaw withdrawal reflex in the rat. J. Neurophysiol 79, 174–180. [PubMed: 9425188]
122. Todd AJ (2010). Neuronal circuitry for pain processing in the dorsal horn. Nat. Rev. Neurosci 11, 823–836. [PubMed: 21068766]
123. Kim J, Back SK, Yoon YW, Hong SK, and Na HS (2005). Dorsal column lesion reduces mechanical allodynia in the induction, but not the maintenance, phase in spinal hemisected rats. Neurosci. Lett 379, 218–222. [PubMed: 15843067]
124. Rankin G, Chirila AM, Emanuel AJ, Zhang Z, Woolf CJ, Drugowitsch J, and Ginty DD (2024). Nerve injury disrupts temporal processing in the spinal cord dorsal horn through alterations in PV^+ interneurons. Cell Rep. 43, 113718. [PubMed: 38294904]
125. Catley MJ, O'Connell NE, Berryman C, Ayhan FF, and Moseley GL (2014). Is tactile acuity altered in people with chronic pain? a systematic review and meta-analysis. J. Pain 15, 985–1000. [PubMed: 24983492]
126. Eriksson NP, Persson JK, Svensson M, Arvidsson J, Molander C, and Aldskogius H (1993). A quantitative analysis of the microglial cell reaction in central primary sensory projection territories following peripheral nerve injury in the adult rat. Exp. Brain Res 96, 19–27. [PubMed: 8243580]
127. Beggs S, Trang T, and Salter MW (2012). P2X4R+ microglia drive neuropathic pain. Nat. Neurosci 15, 1068–1073. [PubMed: 22837036]
128. Salter MW (2005). Cellular signalling pathways of spinal pain neuroplasticity as targets for analgesic development. Curr. Top. Med. Chem 5, 557–567. [PubMed: 16022678]
129. Ueta Y, and Miyata M (2021). Brainstem local microglia induce whisker map plasticity in the thalamus after peripheral nerve injury. Cell Rep 34, 108823. [PubMed: 33691115]
130. Cichon J, Blanck TJJ, Gan W-B, and Yang G (2017). Activation of cortical somatostatin interneurons prevents the development of neuropathic pain. Nat. Neurosci 20, 1122–1132. [PubMed: 28671692]
131. Kim SK, and Nabekura J (2011). Rapid synaptic remodeling in the adult somatosensory cortex following peripheral nerve injury and its association with neuropathic pain. J. Neurosci 31, 5477–5482. [PubMed: 21471384]
132. Xiong W, Ping X, Ripsch MS, Chavez GSC, Hannon HE, Jiang K, Bao C, Jadhav V, Chen L, Chai Z, et al. (2017). Enhancing excitatory activity of somatosensory cortex alleviates neuropathic pain through regulating homeostatic plasticity. Sci. Rep 7, 12743. [PubMed: 28986567]
133. Soleimani B, Board C, Yu T, Tracey I, Irani SR, and Foley P (2023). Immunotherapy-Responsive Neuropathic Pain and Allodynia in a Patient With Glycine Receptor Autoantibodies: A Case Report. Neurol. Neuroimmunol. Neuroinflamm. 10, e200160. [PubMed: 37640544]
134. Lee KY, Ratté S, and Prescott SA (2019). Excitatory neurons are more disinhibited than inhibitory neurons by chloride dysregulation in the spinal dorsal horn. Elife 8, e49753. [PubMed: 31742556]
135. Gradwell MA, Callister RJ, and Graham BA (2020). Reviewing the case for compromised spinal inhibition in neuropathic pain. J. Neural Transm 127, 481–503. [PubMed: 31641856]

136. Guilbaud G, Peschanski M, Gautron M, and Binder D (1980). Neurones responding to noxious stimulation in VB complex and caudal adjacent regions in the thalamus of the rat. Pain 8, 303–318. [PubMed: 7402691]

137. Barbaresi P, and Mensà E (2016). Connections from the rat dorsal column nuclei (DCN) to the periaqueductal gray matter (PAG). Neurosci. Res 109, 35–47. [PubMed: 26902642]

138. Burton H, and Loewy AD (1977). Projections to the spinal cord from medullary somatosensory relay nuclei. J. Comp. Neurol 173, 773–792. [PubMed: 68038]

139. Chen H, Bleimeister IH, Nguyen EK, Li J, Cui AY, Stratton HJ, Smith KM, Baccei ML, and Ross SE (2024). The functional and anatomical characterization of three spinal output pathways of the anterolateral tract. Cell Rep 43, 113829. [PubMed: 38421871]

140. Abraira VE, and Ginty DD (2013). The sensory neurons of touch. Neuron 79, 618–639. [PubMed: 23972592]

141. Choi S, Hachisuka J, Brett MA, Magee AR, Omori Y, Iqbal NUA, Zhang D, DeLisle MM, Wolfson RL, Bai L, et al. (2020). Parallel ascending spinal pathways for affective touch and pain. Nature 587, 258–263. [PubMed: 33116307]

142. Ma W, Peschanski M, and Besson JM (1986). The overlap of spinothalamic and dorsal column nuclei projections in the ventrobasal complex of the rat thalamus: a double anterograde labeling study using light microscopy analysis. J. Comp. Neurol 245, 531–540. [PubMed: 2422226]

143. Brüggemann J, Galhardo V, and Apkarian AV (2001). Immediate reorganization of the rat somatosensory thalamus after partial ligation of sciatic nerve. J. Pain 2, 220–228. [PubMed: 14622820]

144. Lenz FA, Weiss N, Ohara S, Lawson C, and Greenspan JD (2004). The role of the thalamus in pain. In Supplements to Clinical Neurophysiology, 57, Hallett M, Phillips LH, Schomer DL, and Massey JM, eds. (Elsevier), pp. 50–61. [PubMed: 16106605]

145. Yan Y, Zhu M, Cao X, Xu G, Shen W, Li F, Zhang J, Luo L, Zhang X, Zhang D, and Liu T (2023). Thalamocortical Circuit Controls Neuropathic Pain via Up-regulation of HCN2 in the Ventral Posterolateral Thalamus. Neurosci. Bull 39, 774–792. [PubMed: 36538279]

146. Zimmerman AL, Kovatsis EM, Pozsgai RY, Tasnim A, Zhang Q, and Ginty DD (2019). Distinct Modes of Presynaptic Inhibition of Cutaneous Afferents and Their Functions in Behavior. Neuron 102, 420–434.e8. [PubMed: 30826183]

147. Duan B, Cheng L, Bourane S, Britz O, Padilla C, Garcia-Campmany L, Krashes M, Knowlton W, Velasquez T, Ren X, et al. (2014). Identification of spinal circuits transmitting and gating mechanical pain. Cell 159, 1417–1432. [PubMed: 25467445]

148. Harris JA, Mihalas S, Hirokawa KE, Whitesell JD, Choi H, Bernard A, Bohn P, Caldejon S, Casal L, Cho A, et al. (2019). Hierarchical organization of cortical and thalamic connectivity. Nature 575, 195–202. [PubMed: 31666704]

149. Luo W, Enomoto H, Rice FL, Milbrandt J, and Ginty DD (2009). Molecular identification of rapidly adapting mechanoreceptors and their developmental dependence on ret signaling. Neuron 64, 841–856. [PubMed: 20064391]

150. Britz O, Zhang J, Grossmann KS, Dyck J, Kim JC, Dymecki S, Gosgnach S, and Goulding M (2015). A genetically defined asymmetry underlies the inhibitory control of flexor–extensor locomotor movements. Elife 4, e04718. [PubMed: 26465208]

151. Zhou X, Wang L, Hasegawa H, Amin P, Han BX, Kaneko S, He Y, and Wang F (2010). Deletion of PIK3C3/Vps34 in sensory neurons causes rapid neurodegeneration by disrupting the endosomal but not the autophagic pathway. Proc. Natl. Acad. Sci. USA 107, 9424–9429. [PubMed: 20439739]

152. Rutlin M, Ho CY, Abraira VE, Cassidy C, Bai L, Woodbury CJ, and Ginty DD (2015). The Cellular and Molecular Basis of Direction Selectivity of Aδ-LTMRs. Cell 160, 1027. [PubMed: 29698636]

153. Bai L, Lehnert BP, Liu J, Neubarth NL, Dickendesher TL, Nwe PH, Cassidy C, Woodbury CJ, and Ginty DD (2015). Genetic Identification of an Expansive Mechanoreceptor Sensitive to Skin Stroking. Cell 163, 1783–1795. [PubMed: 26687362]

154. Olson W, Abdus-Saboor I, Cui L, Burdge J, Raabe T, Ma M, and Luo W (2017). Sparse genetic tracing reveals regionally specific functional organization of mammalian nociceptors. Elife 6, e29507. [PubMed: 29022879]

155. Cavanaugh DJ, Chesler AT, Jackson AC, Sigal YM, Yamanaka H, Grant R, O'Donnell D, Nicoll RA, Shah NM, Julius D, and Basbaum AI (2011). Trpv1 reporter mice reveal highly restricted brain distribution and functional expression in arteriolar smooth muscle cells. J. Neurosci 31, 5067–5077. [PubMed: 21451044]

156. Hinoi T, Akyol A, Theisen BK, Ferguson DO, Greenson JK, Williams BO, Cho KR, and Fearon ER (2007). Mouse model of colonic adenoma-carcinoma progression based on somatic Apc inactivation. Cancer Res 67, 9721–9730. [PubMed: 17942902]

157. Bourane S, Duan B, Koch SC, Dalet A, Britz O, Garcia-Campmany L, Kim E, Cheng L, Ghosh A, Ma Q, and Goulding M (2015). Gate control of mechanical itch by a subpopulation of spinal cord interneurons. Science 350, 550–554. [PubMed: 26516282]

158. Vong L, Ye C, Yang Z, Choi B, Chua S Jr., and Lowell BB (2011). Leptin action on GABAergic neurons prevents obesity and reduces inhibitory tone to POMC neurons. Neuron 71, 142–154. [PubMed: 21745644]

159. Peron SP, Freeman J, Iyer V, Guo C, and Svoboda K (2015). A Cellular Resolution Map of Barrel Cortex Activity during Tactile Behavior. Neuron 86, 783–799. [PubMed: 25913859]

160. Gorski JA, Talley T, Qiu M, Puelles L, Rubenstein JLR, and Jones KR (2002). Cortical excitatory neurons and glia, but not GABAergic neurons, are produced in the Emx1-expressing lineage. J. Neurosci 22, 6309–6314. [PubMed: 12151506]

161. Madisen L, Garner AR, Shimaoka D, Chuong AS, Klapoetke NC, Li L, van der Bourg A, Niino Y, Egolf L, Monetti C, et al. (2015). Transgenic mice for intersectional targeting of neural sensors and effectors with high specificity and performance. Neuron 85, 942–958. [PubMed: 25741722]

162. Niederkofler V, Asher TE, Okaty BW, Rood BD, Narayan A, Hwa LS, Beck SG, Miczek KA, and Dymecki SM (2016). Identification of Serotonergic Neuronal Modules that Affect Aggressive Behavior. Cell Rep 17, 1934–1949. [PubMed: 27851959]

163. Madisen L, Mao T, Koch H, Zhuo J.m., Berenyi A, Fujisawa S, Hsu YWA, Garcia AJ 3rd, Gu X, Zanella S, et al. (2012). A toolbox of Cre-dependent optogenetic transgenic mice for light-induced activation and silencing. Nat. Neurosci 15, 793–802. [PubMed: 22446880]

164. Daigle TL, Madisen L, Hage TA, Valley MT, Knoblich U, Larsen RS, Takeno MM, Huang L, Gu H, Larsen R, et al. (2018). A Suite of Transgenic Driver and Reporter Mouse Lines with Enhanced Brain-Cell-Type Targeting and Functionality. Cell 174, 465–480.e22. [PubMed: 30007418]

165. Kleinlogel S, Feldbauer K, Dempski RE, Fotis H, Wood PG, Bamann C, and Bamberg E (2011). Ultra light-sensitive and fast neuronal activation with the Ca^{2}+-permeable channelrhodopsin CatCh. Nat. Neurosci 14, 513–518. [PubMed: 21399632]

166. Hughes DI, Sikander S, Kinnon CM, Boyle KA, Watanabe M, Callister RJ, and Graham BA (2012). Morphological, neurochemical and electrophysiological features of parvalbumin-expressing cells: a likely source of axo-axonic inputs in the mouse spinal dorsal horn. J. Physiol 590, 3927–3951. [PubMed: 22674718]

167. Decosterd I, and Woolf CJ (2000). Spared nerve injury: an animal model of persistent peripheral neuropathic pain. Pain 87, 149–158. [PubMed: 10924808]

168. Lee C, and Jones TA (2018). Effects of Ketamine Compared with Urethane Anesthesia on Vestibular Sensory Evoked Potentials and Systemic Physiology in Mice. J. Am. Assoc. Lab. Anim. Sci 57, 268–277. [PubMed: 29784077]

169. Murthy SE, Loud MC, Daou I, Marshall KL, Schwaller F, Kühnemund J, Francisco AG, Keenan WT, Dubin AE, Lewin GR, and Patapoutian A (2018). The mechanosensitive ion channel Piezo2 mediates sensitivity to mechanical pain in mice. Sci. Transl. Med 10, eaat9897. [PubMed: 30305457]

170. Cruccu G, and Truini A (2009). Tools for assessing neuropathic pain. PLoS Med 6, e1000045. [PubMed: 19360134]

171. Hargreaves K, Dubner R, Brown F, Flores C, and Joris J (1988). A new and sensitive method for measuring thermal nociception in cutaneous hyperalgesia. Pain 32, 77–88. [PubMed: 3340425]

172. Prus AJ, James JR, and Rosecrans JA (2009). Conditioned Place Preference (CRC Press/Taylor & Francis).

Highlights

- Gr VPL-PNs and inhibitory neurons receive distinct primary afferent and spinal inputs
- Gr neuronal manipulation bidirectionally alters tactile but not noxious sensitivity
- Increased touch-evoked Gr activation and altered afferent inputs after injury
- Reducing Gr output alleviates tactile hypersensitivity and pain behaviors after injury

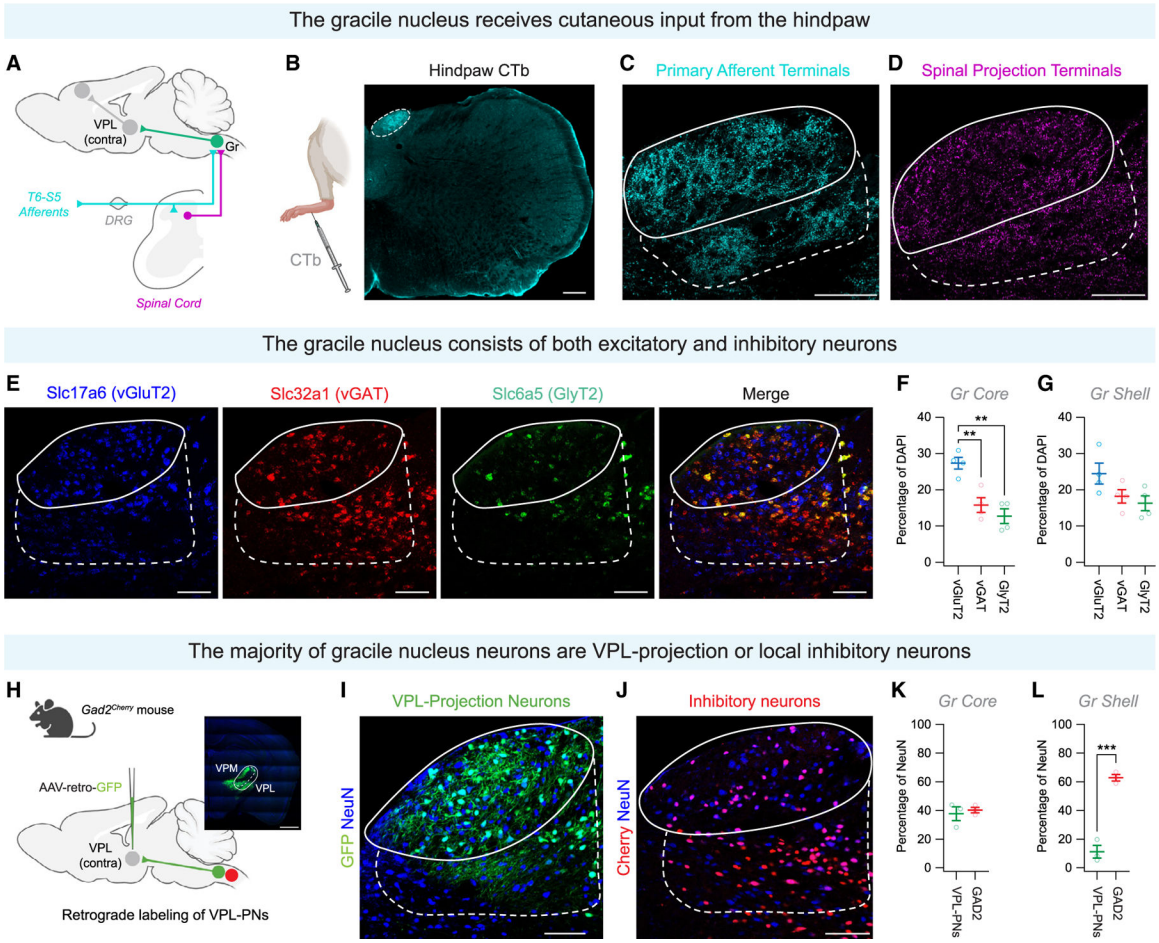

Figure 1. Ascending DRG and spinal pathways converge in the gracile nucleus

(A) The gracile nucleus (Gr, green) receives sensory inputs from lower body DRG afferents (cyan) and spinal projections (magenta). Retrograde virus injections into the VPL (right) labeled Gr VPL-projecting neurons (PNs).

(B) Injection of cholera toxin β subunit (CTb, cyan) into the hindpaw glabrous skin labeled hindlimb afferents targeting the Gr (white dashed circle). Scale bar, 200 μm.

(C) *Advillin*^{Cre}*;Rosa26*$^{LSL\text{-}Synaptophysin\text{-}GFP}$ mice labeled synaptic terminals of primary afferents (cyan) in the Gr core (solid white line) and shell (dashed white line). Scale bar, 100 μm.

(D) *Cdx2*^{Cre}*;Lbx1*^{FlpO}*;Rosa26*$^{LSL\text{-}FSF\text{-}Synaptophysin\text{-}GFP}$ mice labeled terminals of spinal projections (magenta) in the Gr core (solid white line) and shell (dashed white line). Scale bar, 100 μm.

(E) *In situ* hybridization of excitatory (vGluT2, blue) and inhibitory (vGAT, red; GlyT2, green) neurons in the Gr core (solid white line) and shell (dashed white line). Scale bar, 100 μm.

(F and G) Quantification of excitatory and inhibitory neuronal markers in the Gr core (F) and shell (G).

(H) Strategy to label VPL-PNs (green) or inhibitory neurons (red). Inset: representative injection of AAV-retro GFP into the VPL. Scale bar, 1,000 μm.

(I and J) Representative images of Gr VPL-PNs (I) (green), inhibitory neurons (J) (red), and $NeuN^+$ immunostaining of neurons (blue). Scale bar, 100 μm.
(K and L) Quantification of VPL-PNs and inhibitory neurons in the Gr core (K) and shell (L) normalized to total NeuN.

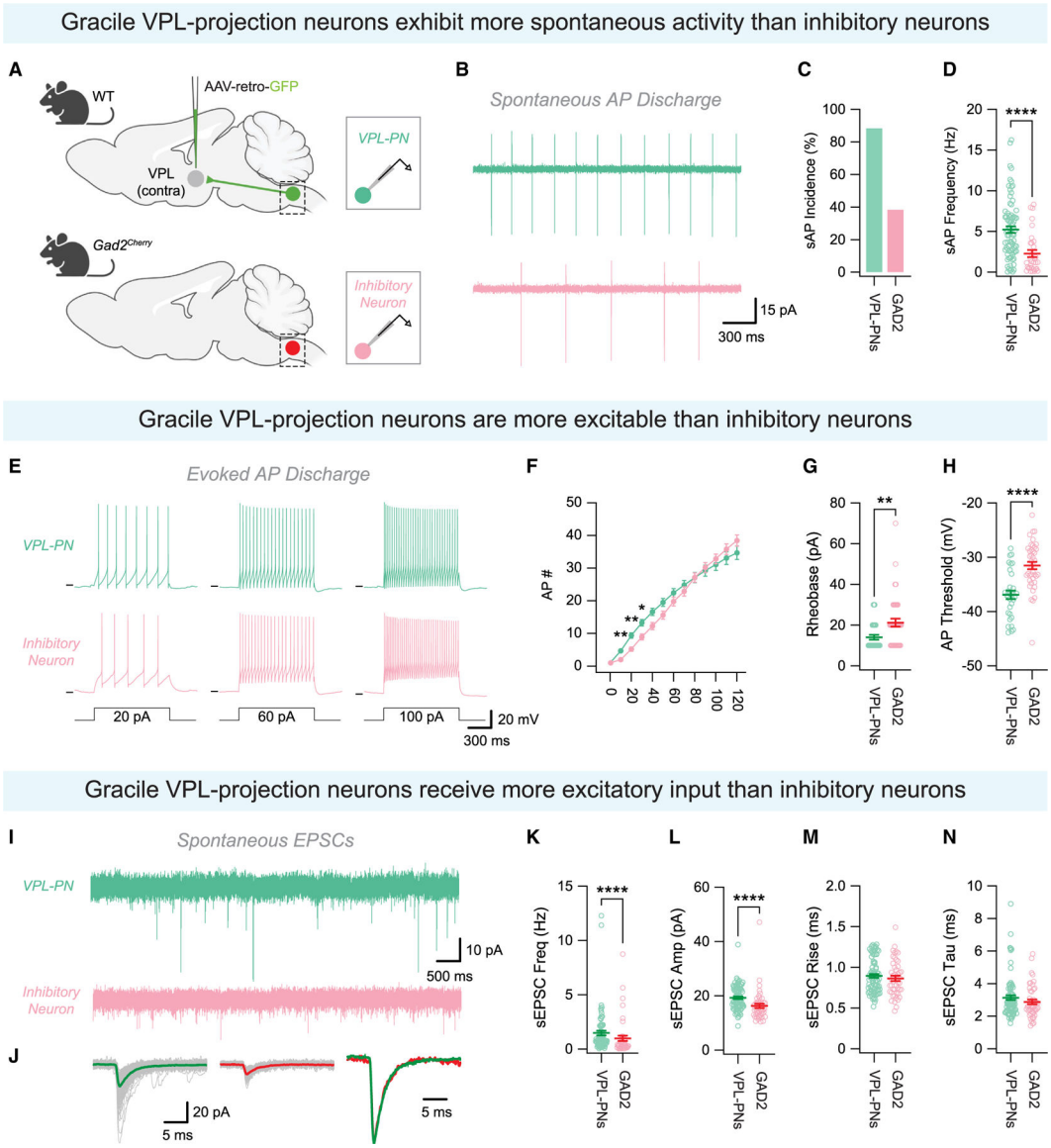

Figure 2. Gr VPL-PNs and inhibitory neurons exhibit different electrophysiological properties and excitatory drive

(A) Labeling of VPL-PNs and inhibitory neurons for slice electrophysiology.

(B) Cell-attached voltage-clamp recordings showing spontaneous AP discharge in VPL-PN (green) and inhibitory neuron (red).

(C) Percentage of neurons exhibiting spontaneous AP discharge.

(D) Quantification of sAP frequency.

(E) Whole-cell current clamp recording (−60 mV) from VPL-PN (green) and inhibitory neuron (red) in response to depolarizing current injection.

(F) Quantification of AP number in response to depolarizing current injection.

(G) Quantification of AP rheobase.

(H) Quantification of AP threshold.

(I) Whole-cell voltage-clamp recordings (−70 mV) of sEPSCs from VPL-PN (green) and inhibitory neuron (red).

(J) Captured sEPSCs from representative cells shown in (I). Right trace shows amplitude normalized overlay.
(K) Quantification of sEPSC frequency.
(L) Quantification of sEPSC amplitude.
(M) Quantification of sEPSC rise time.
(N) Quantification of sEPSC decay time.

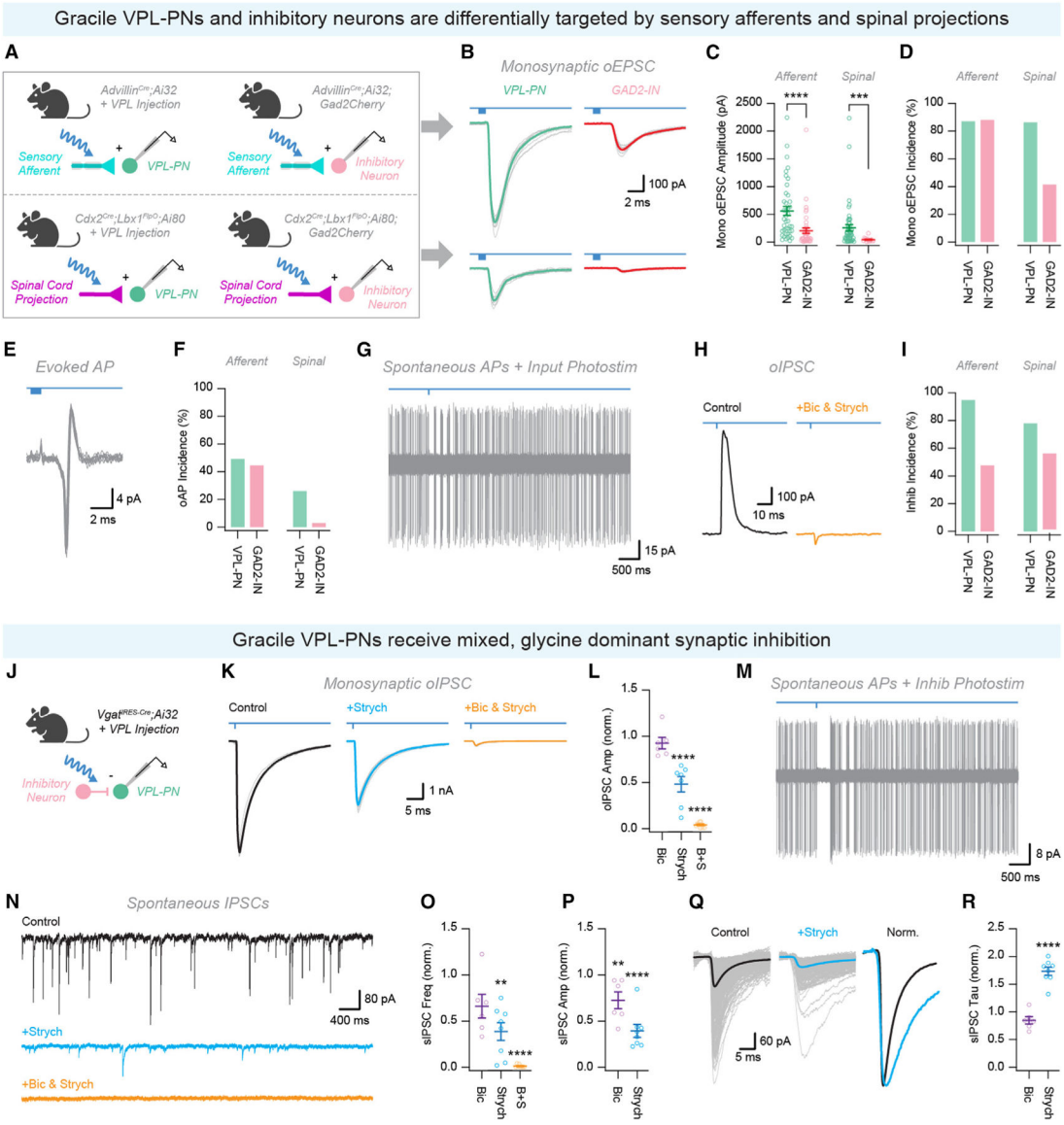

Figure 3. Primary afferent and spinal inputs differentially innervate Gr VPL-PNs and inhibitory neurons and evoke feedforward inhibition

(A) Strategies to optogenetically activate primary afferent or spinal inputs onto Gr VPL-PNs or inhibitory neurons.

(B) Whole-cell voltage-clamp recordings (−70 mV) of optically evoked EPSCs (oEPSCs) from VPL-PN (green) and inhibitory neuron (red) in response to primary afferent (top) and spinal projection (bottom) photostimulation. Ten consecutive sweeps, with average overlaid.

(C) Quantification of monosynaptic oEPSC amplitude.

(D) Percentage of neurons exhibiting monosynaptic oEPSCs.

(E) Cell-attached voltage-clamp recording showing optically evoked AP discharge (sAP). Ten consecutive sweeps overlaid.

(F) Percentage of neurons exhibiting sAP discharge.

(G) Cell-attached voltage-clamp recording showing the impact of optogenetic activation of ascending inputs on spontaneous AP discharge. Ten consecutive sweeps overlaid.

(H) Whole-cell voltage-clamp recordings (−20 mV) of optically evoked IPSCs (oIPSCs) in control (black) and following application of bicuculline (10 μM) and strychnine (1 μM; orange) in response to optogenetic activation of ascending inputs. Ten consecutive sweeps with average overlaid.
(I) Percentage of neurons exhibiting oIPSCs.
(J) Strategy to optogenetically activate inhibitory inputs onto Gr VPL-PNs.
(K) Whole-cell voltage-clamp recordings (−70 mV) of oIPSCs in control (black) and following sequential application of strychnine (1 μM; blue) and bicuculline (10 μM; orange) in response to optogenetic activation of inhibitory neurons. Ten consecutive sweeps, with average overlaid.
(L) Normalized impact of bicuculline (10 μM), strychnine (1 μM), and bicuculline + strychnine application on oIPSC amplitude.
(M) Cell-attached voltage-clamp recording showing the impact of optogenetic activation of inhibitory inputs on spontaneous AP discharge. Ten consecutive sweeps overlaid.
(N) Whole-cell voltage-clamp recordings (−70 mV) of sIPSCs from VPL-PN in control (black) and following sequential application of strychnine (1 μM; blue) and bicuculline (10 μM; orange).
(O) Normalized impact of bicuculline (10 μM), strychnine (1 μM), and bicuculline + strychnine application on sIPSC frequency.
(P) Normalized impact of bicuculline (10 μM), strychnine (1 μM), and bicuculline + strychnine application on sIPSC amplitude.
(Q) Captured sIPSCs from representative cells shown in (N). Right trace shows amplitude normalized overlay.
(R) Normalized impact of bicuculline (10 μM), strychnine (1 μM), and bicuculline + strychnine application on sIPSC decay.

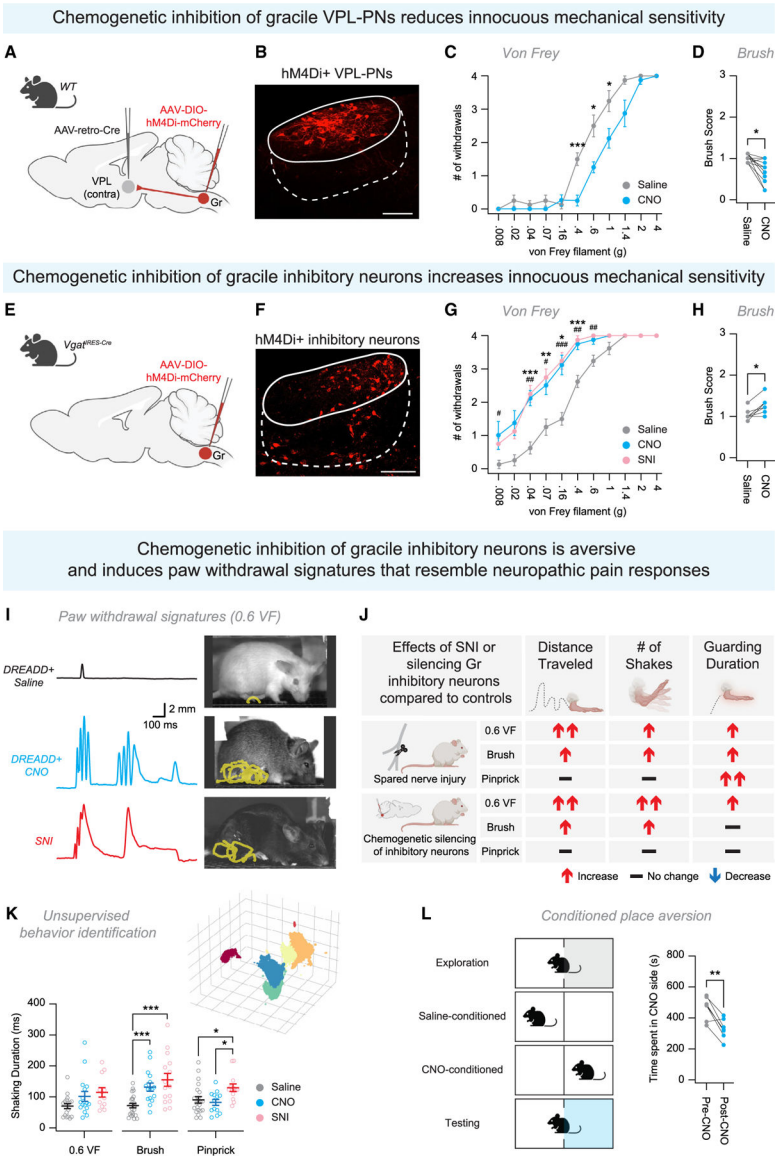

Figure 4. Manipulation of Gr VPL-PNs and inhibitory neuron scales tactile sensitivity and intensity of tactile withdrawal responses

(A and B) Strategy to silence Gr VPL-PNs (red) using CNO, with saline as a control. Scale bar, 100 μm.

(C) Responses to von Frey stimulation when silencing VPL-PNs.

(D) Responses to dynamic brush when silencing VPL-PNs.

(E and F) Strategy to silence Gr inhibitory neurons (red) using CNO, with saline as a control. Scale bar, 100 μm.

(G) Responses to von Frey stimulation when silencing Gr inhibitory neurons.*CNO vs. saline, #SNI vs. saline.

(H) Responses to dynamic brush when silencing Gr inhibitory neurons.

(I) Representative traces of MTP y-coordinates during 0.6-g von Frey stimulation for control mice (black), mice with silenced Gr inhibitory neurons (blue), and SNI mice (red).

(J) Pain Assessment at Withdrawal Speeds (PAWS[91]) analysis for SNI mice and mice where Gr inhibitory neurons were silenced compared to saline control. ↑ represents an increase compared to control mice, ↓ represents a decrease compared to control mice, and – represents no change.

(K) First three dimensions of B-SOiD[92] uniform manifold approximation and projection (UMAP) embedding, showing in low-dimensional space a projection of extracted behavioral features. Colors represent behavioral clusters identified by hierarchical density-based spatial clustering of applications with noise, including a shaking cluster (turquoise).

(L) Conditioned place preference assay to assess appetitive/aversive nature of silencing Gr inhibition.

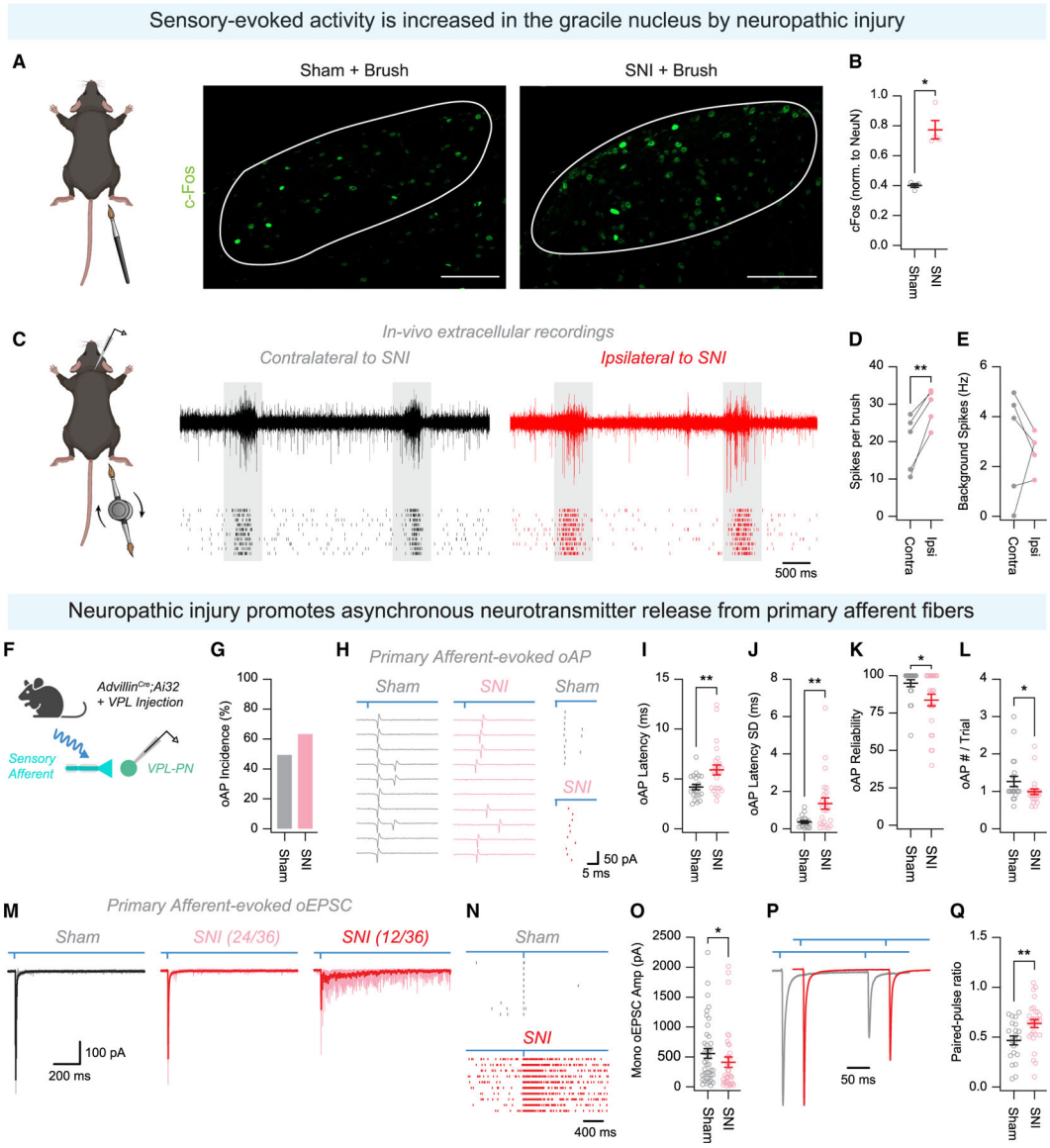

Figure 5. Increased tactile-evoked activity and altered primary afferent drive onto Gr VPL-PNs during neuropathic pain

(A) c-Fos immunolabeling (green) of Gr neurons in response to brush stimulation in anesthetized sham and SNI mice. Scale bar, 100 μm.

(B) Quantification of Fos$^+$ cells (normalized to total NeuN) in response to brush stimulation in anesthetized sham and SNI mice.

(C) Brush-evoked activity (gray boxes) and spontaneous activity (space between boxes) during *in vivo* recordings in anesthetized mice.

(D and E) Quantification of evoked (D) and spontaneous (E) spiking activity.

(F) Approach to activate primary afferent inputs to VPL-PNs.

(G) Percentage of neurons that exhibited an optically evoked AP (oAP) following primary afferent photostimulation.

(H) Cell-attached voltage-clamp recording showing oAP following primary afferent photostimulation in sham (gray) and SNI (red). Ten consecutive sweeps. Right: raster plot of example recordings.
(I) Quantification of first oAP latency.
(J) Quantification of first oAP latency standard deviation.
(K) Quantification of first oAP reliability (percentage of trials in which primary afferent photostimulation elicited an oAP in each cell).
(L) Quantification of the number of oAPs evoked per stimulus (total oAP number/number of trials).
(M) Whole-cell voltage-clamp recordings of oEPSC from VPL-PNs in sham (gray) and SNI (red) mice following primary afferent photostimulation. Ten consecutive sweeps, with average overlaid. Following SNI, one-third of VPL-PNs exhibited prolonged activity after primary afferent photostimulation (right).
(N) Raster plot of EPSC incidence in sham (top) and SNI (bottom) VPL-PNs.
(O) Quantification of oEPSC amplitude.
(P) Whole-cell voltage-clamp recording (−70 mV) from VPL-PNs in sham (gray) and SNI (red) mice showing oEPSC paired-pulse response to primary afferent photostimulation.
(Q) Quantification of oEPSC paired-pulse ratio.

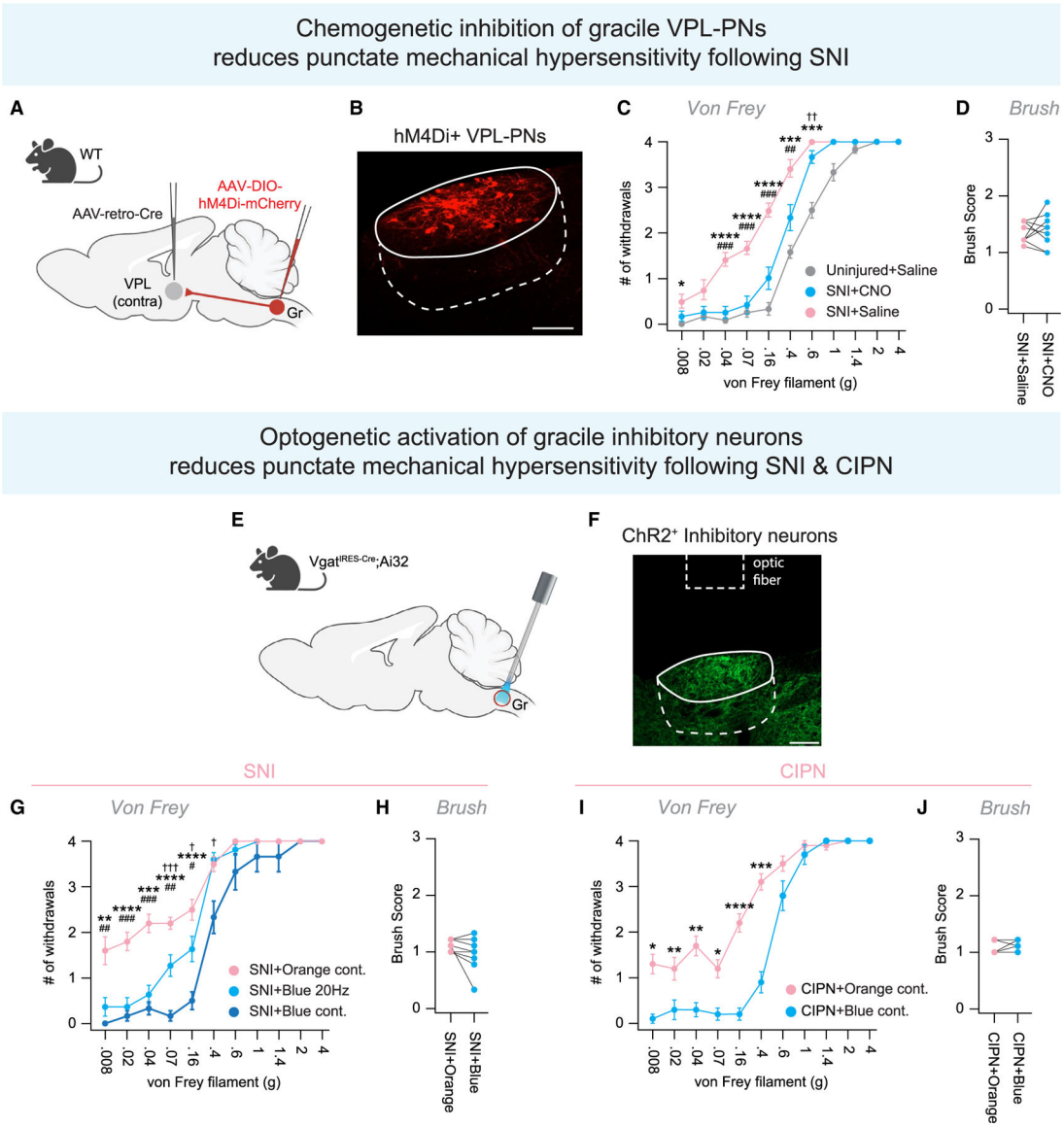

Figure 6. Silencing VPL-PNs or enhancing Gr inhibition specifically alleviates tactile hypersensitivity

(A and B) Strategy to silence Gr VPL-PNs (red) in SNI mice. Scale bar, 100 μm.

(C) Responses to von Frey stimulation when silencing VPL-PNs. *Uninjured + saline vs. SNI + saline; #SNI + saline vs. SNI + CNO; †uninjured + saline vs. SNI + CNO.

(D) Responses to dynamic brush when silencing VPL-PNs in SNI mice.

(E and F) Strategy to optogenetically activate Gr inhibition in SNI and CIPN mice implanted with an optic cannula over the Gr. Blue light activated Gr inhibition, while orange light was used as a control.

(G) Responses to von Frey stimulation when activating Gr inhibition in SNI mice. *Orange control vs. blue control; #orange control vs. blue, 20 Hz; †blue control vs. blue 20 Hz.

(H) Responses to dynamic brush when activating Gr inhibition in SNI mice.

(I) Responses to von Frey stimulation when activating Gr inhibition in CIPN mice.

(J) Responses to dynamic brush when activating Gr inhibition in CIPN mice.

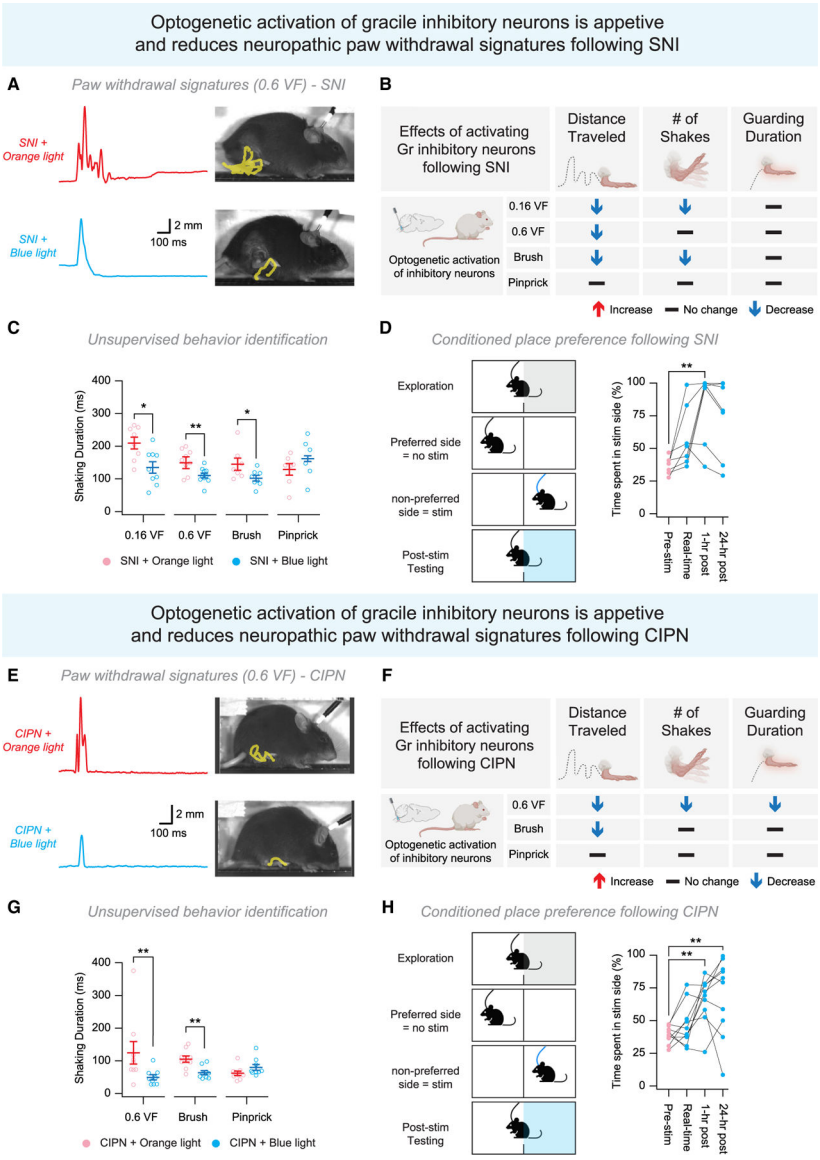

Figure 7. Enhancing Gr inhibition reduces neuropathic paw-withdrawal signatures and induces conditioned place preference

(A) Representative traces of MTP y-coordinates of SNI mice responding to a 0.6-g von Frey stimulus while activating Gr inhibition.

(B) PAWS-identified paw-withdrawal features of SNI mice while activating Gr inhibition. ↑ represents an increase compared to control mice, ↓ represents a decrease compared to control mice, and – represents no change.

(C) Quantification of a B-SOiD-identified shaking behavior while activating Gr inhibition in SNI mice.

(D) Conditioned place preference during activation of Gr inhibition in SNI mice.

(E) Representative traces of MTP y-coordinates of CIPN mice responding to a 0.6-g von Frey stimulus while activating Gr inhibition.

(F) PAWS-identified paw-withdrawal features of CIPN mice while activating Gr inhibition. ↑ represents an increase compared to control, ↓ represents a decrease compared to control, and - represents no change.

(G) Quantification of a B-SOiD-identified shaking behavior while activating Gr inhibition in CIPN mice.

(H) Conditioned place preference during activation of Gr inhibition in CIPN mice.

For all figures, data are reported as mean values ± SEM. *$p \leq 0.05$; **$p \leq 0.01$; ***$p \leq 0.001$; ****$p \leq 0.0001$.

For further details on genetic crosses and statistical tests, see STAR Methods.

KEY RESOURCES TABLE

REAGENT or RESOURCE	SOURCE	IDENTIFIER
Antibodies		
Rabbit anti-Iba1 (1:1000, IHC)	Abcam	Ab178846; RRID:AB_2636859
Chicken anti-GFAP (1:1000, IHC)	MyBioSource	MBS555403; RRID:AB_3675842
Chicken anti-GFP (1:1000, IHC)	Aves	GFP 1020; RRID:AB_2307313
Rabbit anti-GFP (1:1000, IHC)	Invitrogen	A11122; RRID:AB_221569
Mouse anti-NeuN (1:2000, IHC)	Millipore	MAB377; RRID:AB_2298772
Rabbit anti-Neuropeptide Y (1:1000, IHC)	Peninsula Laboratories	T-4070.0050; RRID:AB_518504
Rabbit anti-dsRed (1:2000, IHC)	Takara	632496; RRID:AB_10013483
Rabbit anti-cfos (1:1000, IHC)	Synaptic Systems	226003; RRID:AB_2231974
Goat anti-CTb (1:5000, IHC)	List Biological Labs	703; RRID:AB_10013220
Mouse anti-VGAT (1:2000, IHC)	Synaptic Systems	131011; RRID:AB_887872
Guinea pig anti-VGLUT1 (1:2000, IHC)	Millipore	AB5905; RRID:AB_2301751
Rat anti-substance P (1:1000, IHC)	Bio-Rad	8450-0505; RRID:AB_2200292
Bacterial and viral strains		
pAAV-hSyn-DIO-EGFP (AAV1)	Addgene	50457-AAV1
pAAV1-hSyn-DIO-hM4D(Gi)-mCherry (AAV1)	Addgene	44362-AAV1
pENN.AAV.hSyn.Cre.WPRE.hGH (AAVrg)	Addgene	105553-AAVrg
AAV phSyn1(S)-FLEX-tdTomato-T2A-SypEGFP-WPRE (AAV1)	Addgene	51509-AAV1
pENN.AAV.CB7.CI.eGFP.WPRE.rBG (AAV9)	Addgene	105542-AAV9
pENN.AAV.CB7.CI.mCherry.WPRE.RBG (AAV9)	Addgene	105544-AAV9
pAAV-hSyn-EGFP (AAV1)	Addgene	50465-AAV1
Chemicals, peptides, and recombinant proteins		
Paclitaxel	Sigma	PHR1803
Strychnine hydrochloride	Sigma	S8753
Bicuculline methochloride	Alomone	B-137
CNQX disodium salt	Alomone	C-141
Tetrodotoxin (with citrate)	Cayman Chemical	18660-81-6
4-Aminopyridine	Cayman Chemical	504-24-5
Experimental Models: Organisms/Strains		
Mouse: *Advillin*^{Cre}	Jackson Laboratories	Jax#032536
Mouse: *Advillin*^{FlpO}	Zimmerman et al.[146]	
Mouse: *Cdx2*^{Cre}	Jackson Laboratories	Jax#009350
Mouse: *Emx1*$^{IRES-Cre}$	Jackson Laboratories	Jax#005628
Mouse: *Gad2*^{Cherry}	Jackson Laboratories	Jax#023140
Mouse: *Lbx1*^{FlpO}	Duan et al.[147]	
Mouse: *Mrgprd*^{CreER}	Jackson Laboratories	Jax#031286
Mouse: *Ptgfr*^{CreER}	Lehnert et al.[68]	

REAGENT or RESOURCE	SOURCE	IDENTIFIER
Mouse: *Pvalb*^{2aCreER}	Jackson Laboratories	Jax#028580
Mouse: *Rbp4*^{Cre}	Harris et al.[148]	
Mouse: *Ret*^{CreER}	Luo et al.[149]	
Mouse: *Rosa26*$^{LSL\text{-}FSF\text{-}tdTomato}$	Jackson Laboratories	Ai65, Jax#021875
Mouse: *Rosa26*$^{LSL\text{-}FSF\text{-}synaptophysin\text{-}GFP}$	Jackson Laboratories	*RC::FPSit, FPSit* Jax#030206
Mouse: *Rosa26*$^{LSL\text{-}SynGFP}$	This paper	Derived from Jax#030206
Mouse: *Rosa26*^{LSL}-synaptophysin-tdTomato	Jackson Laboratories	Ai34, Jax#012570
Mouse: *Rosa26*^{LSL}-ChR2-YFP	Jackson Laboratories	Ai32, Jax#024109
Mouse: *Rosa26*^{LSL}-FSF-ChR2-YFP	Jackson Laboratories	Ai80, Jax#025109
Mouse: *Split*^{Cre}	Abraira et al.[61]	
Mouse: *Tau*$^{ds\text{-}DTR}$	Britz et al.[150]	
Mouse: *Nrtk2*^{CreER} (aka *Trkb*^{CreER})	Jackson Laboratories	Jax#027214
Mouse: *Nrtk3*^{CreER} (aka *Trkc*^{CreER})	Jackson Laboratories	Jax#030291
Mouse: *Trpv1*^{Cre}	Jackson Laboratories	Jax#017769
Mouse: *Th*^{2aCreER}	Jackson Laboratories	Jax#025614
Mouse: *Vgat*$^{IRES\text{-}Cre}$	Jackson Laboratories	Jax#028862
Oligonucleotides		
vGAT	ACD Biosciences	319191
vGluT2	ACD Biosciences	456751
GlyT2	ACD Biosciences	409741
Software and algorithms		
AxoGraph		https://axograph.com/
p-CLAMP 11	Molecular Devices	https://www.moleculardevices.com/products/axon-patch-clamp-system/acquisition-and-analysis-software/pclamp-software-suite
ImageJ		https://imagej.nih.gov/ij/
IMARIS	Oxford Instruments	https://imaris.oxinst.com/
Adobe Illustrator	Adobe	https://www.adobe.com/
Prism	GraphPad	www.graphpad.com
DeepLabCut	Mathis et al.[97]	https://github.com/DeepLabCut/DeepLabCut
PAWS	Jones et al.[91]	https://github.com/crtwomey/paws
B-SOiD	Hsu et al.[92]	https://github.com/YttriLab/B-SOID